Supercooled liquid water clouds observed over Dome C, Antarctica: temperature sensitivity and surface radiation impact

Philippe Ricaud[1], Massimo Del Guasta[2], Angelo Lupi[3], Romain Roehrig[1], Eric Bazile[1], Pierre Durand[4], Jean-Luc Attié[4], Alessia Nicosia[3] and Paolo Grigioni[5]

[1]CNRM, Université de Toulouse, Météo-France, CNRS, Toulouse, France (philippe.ricaud@meteo.fr; romain.roehrig@meteo.fr; eric.bazile@meteo.fr)

[2]INO-CNR, Sesto Fiorentino, Italy (massimo.delguasta@ino.cnr.it)

[3]ISAC-CNR, Bologna, Italy (a.lupi@isac.cnr.it; a.nicosia@isac.cnr.it)

[4]Laboratoire d'Aérologie, Université de Toulouse, CNRS, UPS, Toulouse, France (pierre.durand@aero.obs-mip.fr; jean-luc.attie@aero.obs-mip.fr)

[5]ENEA, Roma, Italy (paolo.grigioni@enea.it)

Correspondence: philippe.ricaud@meteo.fr

~~21 October~~~~1~~14 December 2022, Version REV01 V01

~~To be s~~Submitted to **Atmospheric Chemistry and Physics**

Abstract

Clouds affect the Earth climate with an impact that depends on the cloud nature (solid/ liquid water). Although the Antarctic climate is changing rapidly, cloud observations are sparse over Antarctica due to few ground stations and satellite observations. The Concordia station is located on the East Antarctic Plateau (75°S, 123°E, 3233 m above mean sea level), one of the driest and coldest places on Earth. We used observations of clouds, temperature, liquid water and surface radiation performed at Concordia during 4 austral summers (December 2018-2021) to analyse the link between liquid water and temperature and its impact on surface radiation in the presence of supercooled liquid water (liquid water for temperature less than 0°C) clouds (SLWCs). Our study has shown that, at the Concordia station, the very local structure of the ice surface highly impacts the surface albedo and therefore the radiation budget. The ERA5 or CERES data are not able to reproduce the diurnal variation of the local albedo. We established that a two-sine empirical function with 24-h and 12-h periods well fits the BSRN observed albedo. We show that ground-based observations are likely the best way to estimate the Net SR in Concordia. Our analysis shows that, within SLWCs, temperature logarithmically increases from -36.0°C to -16.0°C when liquid water path increases from 1.0 to 14.0 g m^{-2}, and SLWCs positively impact the net surface radiation, which logarithmically increases by 0.0 to 50.0 W m^{-2} when liquid water path increases from 1.7 to 3.0 g m^{-2}. We finally estimate that SLWCs have a great potential radiative impact over Antarctica whatever the season considered, up to 5.0 W m^{-2} over the Eastern Antarctic Plateau and up to 30 W m^{-2} over the Antarctic Peninsula in summer.

1. Introduction

Antarctic clouds play an important role in the climate system by influencing the Earth's radiation balance, both directly at high southern latitudes and, indirectly, at the global level through complex teleconnections (Lubin et al., 1998). However, in Antarctica, ground stations are mainly located on the coast and yearlong observations of clouds and associated meteorological parameters are scarce. Meteorological analyses and satellite observations of clouds can nevertheless give some information on cloud properties suggesting that clouds vary geographically, with a fractional cloud cover ranging from about 50 to 60% around the South Pole to 80-90% near the coast (Bromwich et al., 2012; Listowski et al., 2019). In situ aircraft measurements performed mainly over the Western Antarctic Peninsula (Grosvenor et al., 2012; Lachlan-Cope et al., 2016) and nearby coastal areas (O'Shea et al., 2017) provided new insights to polar cloud modelling and highlighted sea-ice production of Cloud-Condensation Nuclei and Ice Nucleating Particles (see e.g. Legrand et al., 2016). Mixed-phase clouds (made of solid and liquid water) are preferably observed near the coast (Listowski et al., 2019) with larger ice crystals and water droplets (Lachlan-Cope, 2010; Lachlan-Cope et al., 2016; Grosvenor et al., 2012; O'Shea et al., 2017; Grazioli et al., 2017). Based on the raDAR/liDAR-MASK (DARDAR) spaceborne products (Listowski et al., 2019), it has been found that clouds are mainly constituted of ice above the continent. ~~whereas t~~The abundance of Supercooled Liquid Water (SLW, the water staying in liquid phase below 0°C) clouds depends on temperature and liquid/ice fraction. It~~,~~ decreases sharply poleward, and is two to three times lower over the Eastern Antarctic Plateau than over the Western Antarctic. An important point remains the inability of both research and operational weather prediction models to accurately represent the clouds (especially SLW clouds, SLWCs) in Antarctica causing biases of several tens W m^{-2} on net surface radiation (Listowski and Lachlan-Cope, 2017; King et al., 2006, 2015; Bromwich et al., 2013) over and beyond the Antarctic (Lawson and Gettelman, 2014; Young et al. 2019).

From year-long LIDAR observations of mixed-phase clouds at South Pole (Lawson and Gettelman, 2014), SLWCs were shown to occur more frequently than in earlier aircraft observations or weather model simulations, leading to biases in the surface radiation budget estimates.

Liquid water in clouds may occur in supercooled form ~~through heterogeneous nucleation~~ due to a relative lack of ice nuclei for temperature greater than -39°C and less than 0°C. Very little SLW is then expected because the ice crystals that form in this temperature range will grow at the expense of liquid droplets (called the "Wegener-Bergeron-Findeisen" process; Wegener, 1911; Bergeron, 1928; Findeisen, 1938; Storelvmo and Tan, 2015). Nevertheless, SLW is often observed at negative temperatures higher than -20°C at all latitudes being a danger to aircraft since icing on the wings and airframe can occur, reducing lift, and increasing drag and weight. As temperature decreases to -36°C, SLW dramatically lessens, so it is highly difficult 1) to observe SLWCs and 2) to quantify the amount of liquid water present in SLWCs. But during the Year Of Polar Prediction (YOPP) international campaign, recent observations performed at the Dome C station in Antarctica of 2 case studies in December 2018 have revealed SLWCs with temperature between -20°C and -30°C and Liquid Water Path (LWP, the liquid water ~~concentration~~ content integrated along the vertical) between 2 to 20 g m^{-2}, as well as a considerable impact on the net Surface Radiation (SR) that exceeded the simulated values by 20-50 W m^{-2} (Ricaud et al., 2020).

The Dome C (Concordia) station, jointly operated by French and Italian institutions in the Eastern Antarctic Plateau (75°06'S, 123°21'E, 3233 m above mean sea level, amsl), is one of the driest and coldest places on Earth with surface temperatures ranging from about -20°C in summer to -70°C in winter. There are three main instruments relevant to this study that have been routinely running for about 10 years: 1) The H_2O Antarctica Microwave Stratospheric and Tropospheric Radiometer (HAMSTRAD, Ricaud et al., 2010a) to obtain vertical profiles of temperature and water vapour, as well as the LWP. 2) The tropospheric depolarization LIDAR (Tomasi et al., 2015) to obtain vertical profiles of backscatter and depolarization to be used for the detection of SLWCs. 3) The Baseline Surface Radiation Network (BSRN) station to measure surface longwave (4–50 µm) and shortwave (0.3–3 µm), downward and upward radiation surface radiation (SR) from which the Net Surface Radiation (Net SR)SR, calculated as the difference between the downward and upward SRs, can be computed (Driemel et al., 2018) as:

$$\text{Net SR} = \text{LWD SR} - \text{LWU SR} + \text{SWD SR} - \text{SWU SR} \quad (1)$$

where LWD SR, LWU SR, SWD SR and SWU SR correspond to Longwave Downward, Longwave Upward, Shortwave Downward and Shortwave Upward SRs, respectively. Hereafter, we will use either the term “radiative flux” or “radiation”, the latter consistent with the terminology presented page 256 ofby Stull (20121988).

The article is structured as follows. Section 2 presents the instruments during the period of study. In section 3, we detail the methodology employed to detect the SLWCs and calculate their impact on SR, and we present the statistical method to emphasize the relationship between temperature and LWP on one hand, and SR and LWP on the other hand. The results are highlighted in section 4 and discussed in section 5, before concluding in section 6.

2. Instruments

We have used the observations from 3 instruments held at the Dome C station, namely the LIDAR instrument to classify the cloud as SLWC, the HAMSTRAD microwave radiometer to obtain LWP and vertical profiles of temperature, and Liquid Water Path (LWP) and the BSRN network to measure the Surface Radiation (SR) components: LWD, LWU, SWD and SWU to finally obtain the Net SR.

2.1. LIDAR

The tropospheric depolarization LIDAR (532 nm) has been operating at Dome C since 2008 (see http://lidarmax.altervista.org/englidar/_Antarctic%20LIDAR.php). The LIDAR provides 5-min tropospheric profiles of ~~aerosols and~~ clouds characteristics continuously, from 20 to 7000 m above ground level (agl), with a resolution of 7.5 m. For the present study, the most relevant parameter is the LIDAR depolarization ratio (Mishchenko et al., 2000) that is a robust indicator of non-spherical shape for randomly oriented cloud particles. A depolarization ratio below 10% is characteristic of SLWC, while higher values are produced by ice particles. The possible ambiguity between ~~SLWC~~ SLW droplets and oriented ice plates is avoided at Dome C by operating the LIDAR 4° off-zenith (Hogan and Illingworth, 2003).

2.2. HAMSTRAD

HAMSTRAD is a microwave radiometer that profiles water vapour, liquid water and tropospheric temperature above Dome C. Measuring at both 60 GHz (oxygen molecule line (O_2) to deduce the temperature) and 183 GHz (H_2O line), this unique, state-of-the-art radiometer was installed on site for the first time in January 2009 (Ricaud et al., 2010a and b). The measurements of the HAMSTRAD radiometer allow the retrieval of the vertical profiles of water vapour and temperature from the ground to 10-km altitude with vertical resolutions of 30 to 50 m in the Planetary Boundary Layer (PBL), 100 m in the lower free troposphere and 500 m in the upper troposphere-lower stratosphere. The time resolution is adjustable and fixed at 60 seconds since 2018. Note that an automated internal calibration is performed every 12 atmospheric observations and lasts about 4 minutes. Consequently, the atmospheric time sampling is 60 seconds for a sequence of 12 profiles and a new sequence starts 4 minutes after the end of the previous one. The temporal resolution on the instrument allows for detection and analysis of atmospheric processes such as the diurnal evolution of the PBL (Ricaud et al., 2012) and the presence of clouds and diamond dust (Ricaud et al., 2017) together with SLWCs (Ricaud et al., 2020). In addition, the LWP (g m^{-2}) that gives the amount of liquid water integrated along the vertical can also be estimated. Observations of LWP have been performed when the instrument was installed at the Pic du Midi station (2877 amsl, France) during the calibration/validation period in 2008 prior to its set up in Antarctica in 2009 (Ricaud et al., 2010a) and during the Year Of Polar Prediction (YOPP) campaign in summer 2018-2019 (Ricaud et al., 2020). At the present time, it has not yet been possible to compare HAMSTRAD LWP retrievals with observations from other instruments, neither at the Pic du Midi nor at Dome C stations. To better evaluate its performance, the 2021-2022 and the future 2022-2023 summer campaigns are dedicated to in-situ observations of SLWCs. Comparisons with numerical weather prediction models were showing consistent amounts of LWP at Dome C when the partition function between ice and liquid water was favouring SLW for temperatures less than 0°C (Ricaud et al., 2020). Note that microwave observations at 60 and 183 GHz are not sensitive to ice crystals. This has already been discussed in Ricaud et al. (2017) when considering the study of diamond dust in Antarctica. As a consequence, possible precipitation~~s~~ of ice, within or below~~in the presence of~~ SLW clouds, as detected by the Lidar, does not affect the retrievals of temperature, water vapour and liquid water.

2.3. BSRN

The BSRN sensors at Dome C are mounted at the Astroconcordia/Albedo-Rack sites, with upward and downward looking, heated and ventilated Kipp&Zonen CM22 pyranometers and CG4 pyrgeometers providing measurements of hemispheric downward and upward broadband shortwave (SW, 0.3–3 µm) and longwave (LW, 4–50 µm) radiative fluxes at the surface, respectively. These data are used to retrieve values of net surface radiation. All these measurements follow the rules of acquisition, quality check and quality control of the BSRN (Driemel et al., 2018).

2.4. Period of study

From the climatological study presented in Ricaud et al. (2020), the SLWCs are mainly observed above Dome C in summer, with a higher occurrence in December than in January: 26% in December against 19% in January representing the percentage of days per month that SLW clouds were detected during the YOPP campaign (summer 2018-2019) within the LIDAR data for more than 12 hours per day. We have thus concentrated our analysis on December and the 4 years: 2018-2021. Since we have to use the three data sets (LIDAR, HAMSTRAD and BSRN) in time coincidence, the actual number of days per year selected in our analysis is presented in Table 1.

3. Methodology

3.1. SLWC detection and Surface Radiation Impact

Consistent with Ricaud et al. (2020), we use LIDAR observations to discriminate between SLW and ice in a cloud. High values of LIDAR backscatter coefficient ($\beta > 100\ \beta_{mol}$, with β_{mol} the molecular backscatter) associated with very low depolarization ratio (< 5%) signifies the presence of an SLWC whilst high depolarization ratio (>20%) indicates the presence of an ice cloud or precipitation. Once the SLWC is detected both in time and altitude, the regular temperature (θ) profile within the cloud and the LWP measured by the HAMSTRAD radiometer in time coincidence are selected together with the SR observed by the BSRN instruments: Net, LWD, LWU, SWD and SWU SR.

The Lidar ~~observations retrieved along the vertical~~profiles are ~~vertically~~ interpolated along the temperature vertical grid and then ~~time interpolated along the~~ according to the temperature time ~~grid~~sampling. As a consequence, for a given time and height, we have a depolarization ratio, a backscatter signal, a regular temperature and a (not height-dependent) LWP. The same method is used for SR. BSRN SRs are time interpolated to be coincident with the LWP values. So, for a given time, we have a set of BSRN SRs (Net, LWU, LWD, SWU and SWD) and an LWP. At a (time, height) point showing high backscatter signal and low depolarization, the associated parameters (regular temperature, LWP and SRs) are flagged as “SLW cloud”. The statistic is thus done using all the SLW-flagged points without any averaging. The temperature corresponds to the in-cloud temperature.

Figure 1 shows, as a typical example, the time evolution of the LIDAR backscatter coefficient and depolarization ratio, as well as the HAMSTRAD LWP and temperature vertical profile for the 27 December 2021. Associated with these SLWCs, the LWP increases with time from 1.0 to 3.0 g m^{-2}. The SLWCs are present over a temperature range varying from about -28.0 °C to -33.0 °C. Note the cloud present at 04:00-05:00 UTC that is not labelled as a SLWC but rather as an ice cloud (high backscatter and high depolarization signals) with no associated increase of LWP and temperature above -28.0 °C.

Figure 2 highlights the time evolution of the SLWC obtained on 27 December 2021 together with some snapshots from the HALO-CAM video camera taken with or without SLWC on: 01:00 (no SLWC), 07:19 (SLWC), 09:00 (no SLWC), 10:14 (SLWC), 13:00 (no SLWC), 16:03 (SLWC), 18:01 (no SLWC) and 20:53 UTC (SLWC). SLWCs (high backscatter and low depolarization signals) are clearly detected at 07:00-08:00, 10:00-11:00, 16:00-17:00, 21:00-22:00 and 23:00-24:00 UTC over an altitude range 500-1000 m above ground level (agl). In general, SLWCs observed over the station did not correspond to overcast conditions.

Over the 4 summers (December 2018-2021), we have selected 3 datasets in time coincidence with SLWC: LWP, θ and SR. In order to estimate the impact of the SLWC onto the SR, we calculated the anomaly of the daily SR with respect to the clear-sky SR associated to the same day. Since it is impossible to measure for the same day the SR with and without cloud, we have in priority looked for clear-sky days over the months of Decembers in the 20178-2021 period. Since it is impossible to measure for the same day the SR with and without cloud, we have considered, over the 4-summer period, clear-sky 24-hour periods. Only 5 clear-sky days were selected on: 2 and 19 December 2018, and 3, 17 and 26 December 2021. We have considered tThese 5 days, considered as the reference SRs (SR_{Ref}), are presented in Figure 3. We have also calculated (Figure 4) the time evolution of the clear-sky surface radiation variability (δSR_{Ref}), namely the difference in SR observed by the BSRN instruments between each of 5 clear-sky day and the corresponding values averaged over the 5 days, for Net, LWD, LWU, SWD and SWU SR. The SR_{Ref} for the 5 days shown Figure 3 are all consistent to each other with an obvious diurnal cycle in Net, LWD, LWU, SWD and SWU SR (we recall that in December there is a 24-h solar illumination at Dome C). The variability within the 5 days (δSR_{Ref}) shown Figure 4 is within ±20 W m^{-2} for the Net SR with a greater Net SR in 2018 than in 2021, within ±35 W m^{-2} for LWD and LWU SR (maxima on 17 December 2021 and minima on 2 December 2018), and within ±25 W m^{-2} for SWD and SWU SR (maxima on 26 December 2021 and minima on 2 December 2018).

Based on these 5 SR_{Ref}, we performed a systematic study over the 4-summer period by calculating the surface radiation anomaly ΔSR defined as:

$$\Delta SR = SR - SR_{Ref} \tag{2}$$

for Net, LWD, LWU, SWD and SWU. As an example, we show in Figure 5 the time evolution for 27 December 2021 of the presence of the SLWC together with ΔSR calculated with respect to SR_{Ref} set to 26 December 2021. Associated with the SLWC, LWD and LWU ΔSR increase by 30-50 and 10-30 W m^{-2}, respectively, whilst SWD and SWU ΔSR decrease by 50-150 W m^{-2}, respectively. The effect on the Net ΔSR is positive (10-100 W m^{-2}) at 07:00-08:00, 10:00-11:00, 16:00-17:00 UTC and negative (from -30 to -100 W m^{-2}) at 21:00-22:00 and 23:00-24:00 UTC. Note that spikes appear in Net ΔSR, SWU ΔSR and SWD ΔSR mainly during scattered conditions and when large cloud episodes appear or disappear. They are real and can possibly come from the inhomogeneity of the cloud distribution. We thus want to statistically analyse all the ΔSR calculated in 2018-2021 with the 5 SR_{Ref} in order to check whether the net effect of the SLWC on the SR is positive or negative and to evaluate its sensitivity to liquid water amounts.

3.2. Statistical Method

The datasets are binned into 1°C-wide bins for θ, 0.2 g m^{-2}-wide bins for LWP, and 5 W m^{-2}-wide bins for ΔSR. The number of points per bin is calculated for all the paired datasets, namely θ-LWP, and ΔSR-LWP (Net ΔSR-LWP, LWD ΔSR-LWP, LWU ΔSR-LWP, SWD ΔSR-LWP and SWU ΔSR-LWP). The 2D ~~distribution of the Probability~~ probability ~~Density~~ density ~~Function~~ (PD~~F~~) is calculated for the paired datasets and defined as $PD\cancel{F}_{ij} = 100\,\frac{N_{ij}}{N_t}$, where N_{ij} and N_t are the count number in the bin *ij* and the total count number ($N_t = \sum_{j=1}^{N}\sum_{i=1}^{M} N_{ij}$), respectively, with *M* and *N* being the total number of bins in LWP on one side, and in temperature or ΔSR on the other side, respectively. This study is focused on the evaluation of the LWP sensitivity for a given temperature and for a given radiation component (Net, LWD, LWU, SWD, SWU). So, f~~F~~or each value of θ_j (within a 1°C-wide bin *j*) or ΔSR_j (within a 5 W m^{-2}-wide bin *j*), a weighted average of LWP ($\overline{LWP_j}$) is calculated together with its associated weighted standard deviation (σ_{LWP_j}), considering all the LWP_{ij} values (within 0.2 g m^{-2}-wide bins) from *i*=1 to *M*, with *M* the total number of LWP bins and w_{ij} the weight, namely the number of points ($w_{ij} = N_{ij}$), associated to the bin *ij*:

$$\overline{LWP_j} = \frac{\sum_{i=1}^{M} w_{ij}\, LWP_{ij}}{\sum_{i=1}^{M} w_{ij}} \qquad (3)$$

and

$$\sigma_{LWP_j} = \sqrt{\frac{\sum_{i=1}^{M} w_{ij}\,(LWP_{ij} - \overline{LWP_j})^2}{\sum_{i=1}^{M} w_{ij}}} \qquad (4)$$

For each θ and ΔSR dataset, the distribution of the total count numbers N_{tj} per 1°C or 5 W m^{-2} wide bin ($N_{tj} = \sum_{i=1}^{M} N_{ij}$ with j = 1, …, N) can be fitted by a function $N(x)$, with $x = \theta$ or ΔSR, based on 2 to 3 Gaussian distributions as:

$$N(x) = \sum_{k=1}^{2 \text{ or } 3} a_k \exp\left(-\frac{1}{2}\left(\frac{x-\mu_k}{\sigma_k}\right)^2\right) + c \quad (5)$$

with a_k, μ_k and σ_k being the amplitude, the mean and the standard deviation of the k^{th} Gaussian function (k = 1, 2 or 3) and c is a constant. We have used k = 2 for ΔSR and k = 3 for θ. Table 2 lists all the fitted parameters (a_k, μ_k, σ_k and c with k = 1 to 2 or 3).

In the relationship between x (θ or ΔSR) and LWP, we have considered x_j (θ_j or ΔSR_j) to be significant when:

~~$x_j \leq \mu_k \pm \sigma_k$~~ $|x_j - \mu_k| \leq \sigma_k$ for k = 1 ~~or~~ – 2 (for ΔSR) or 1 – 3 (for θ) (6)

and ~~highlighted~~ used for this significant point ~~by showing the~~its ~~associated~~ average value and standard deviation, $\overline{LWP_j}$ and σ_{LWP_j}, respectively, with j = 1, …, N.

Finally, a logarithmic function of the form

$$x = a + b\ln(\overline{LWP}) \quad (7)$$

has been fitted onto these significant points ~~$(\overline{LWP_j} \pm \sigma_{LWP_j}, x_j)$~~ where the retrieved constants a and b are shown in Table 3 for x being θ, Net ΔSR, LWD ΔSR, LWU ΔSR, SWD ΔSR and SWU ΔSR.

4. Results

4.1. Temperature-Liquid Water Relationship in Supercooled Liquid Water Clouds

The relationship between temperature and LWP within SLWCs over the 4-summer period at Dome C is presented Figure 6 left in the form of a Probability Density ~~Function (PDF)~~ that is the fraction of points within each bin of 0.2 g m^{-2} width in LWP and 1.0°C width in temperature. It clearly shows a net tendency for liquid water to increase with temperature, up to ~14 g m^{-2} in LWP and -18°C in temperature, with two zones having a density as high as ~2%, at [0.5 g m^{-2}, -33°C] and [1.5 g m^{-2}, -32°C]. We have performed a weighted average of the LWPs within each temperature bin (Figure 6 centre). Then, we have fitted 3 Gaussian distributions to the count numbers as a function of temperature (Figure 6 right). If we now only consider temperature bins within one-sigma of the centre of the Gaussian distributions, we can fit the following logarithmic relation of the temperature θ as a function of LWP within the SLWC (Figure 6 centre):~~Performing a weighted average of the LWPs within each temperature bin (Figure 6 centre), fitting a Gaussian distribution of the count numbers as a function of temperature (Figure 6 right) and considering only temperature bins within one-sigma of the centre of the Gaussian distributions, we can fit the following logarithmic relation of the temperature θ as a function of LWP within the SLWC (Figure 6 centre):~~

$$\theta(LWP) = -33.8\ (\pm 1.5) + 6.5\ \ln(LWP) \quad (8)$$

for $\theta \in [-36; -16]$ °C and $LWP \in [1.0; 14.0]$ g m^{-2}, where (± 1.5 °C) corresponds to the range where the relationship is valid within the 2 blue dashed lines in Figure 6 centre. In other words, based on our study, we have a clear evidence that supercooled liquid water content exponentially increases with temperature. Considering the temperature vs. LWP relationship, the 2 main Gaussian distributions are centred around -28°C and -30°C, corresponding to temperatures usually encountered in Concordia whilst the third one, far much less intense, is centred around -18°C, probably the signature of very unusual events occurring in Concordia as the warm-moist events. Episodes of warm-moist intrusions exist above Concordia originated from mid-latitudes (Ricaud et al., 2017 and 2020) and are known as “atmospheric rivers” (Wille et al., 2019). Although they are infrequent, they can provide high values of temperature and LWP. ~~Although the amount of LWP is very low (<< 20 g m^{-2}) at Dome C compared to what can be measured and modelled (Lemus et al., 1997) in the Arctic (50-75 g m^{-2}) and at~~

~~middle/tropical latitudes (100-150 g m^{-2}), we intended to estimate its impact on the SR at Dome C.~~

4.2. Impacts of Supercooled Liquid Water Clouds on Surface Radiation

Although the amount of LWP is very low ($\ll$ 20 g m^{-2}) at Dome C compared to what can be measured and modelled (Lemus et al., 1997) in the Arctic (50-75 g m^{-2}) and at middle/tropical latitudes (100-150 g m^{-2}), we intended to estimate its impact on the SR at Dome C. In Figures 7 to 9, the left panel presents the ~~PDF Probability Densities~~PDs (for bins of 0.2 g m^{-2} width in LWP and 5 W m^{-2} width in ΔSR) of the surface radiation anomaly ΔSR as a function of the LWP, for Net, LWD, LWU, SWD and SWU, respectively. The central panel shows, for the same parameters, the corresponding weighted average LWP within 5 W m^{-2}-wide bins of radiation anomaly whereas the right panel shows the corresponding count number within 5 W m^{-2}-wide bins fitted by 2 Gaussian distributions.

Based on our analysis, the relationship between Net ΔSR (in W m^{-2}) and the LWP (in g m^{-2}) has been estimated from the HAMSTRAD and BSRN data as:

$$Net\ \Delta SR(LWP) = -50.0\ (\pm 10.0)\ + 90.0 \ln(LWP) \quad (9)$$

for $Net\ \Delta SR \in [-15; 50]$ W m^{-2} and $LWP \in [1.5; 3.0]$ g m^{-2}, where ($\pm$10.0 W m^{-2}) corresponds to the range where the relationship is valid within the 2 blue dashed lines in Figure 7 centre. Thus, for LWP greater than 1.7 g m^{-2}, our study clearly shows that there is a positive impact of SLWC on the Net ΔSR that can reach 50 W m^{-2} for an LWP of 3.0 g m^{-2}.

The splitting of the net radiation anomaly between each of its four components can be evaluated from their individual relationships with the LWP. These relations are gathered in Table 3, established from the plots presented in Figures 7 to 9. They are of the same form as for net surface radiation anomaly, i.e. a logarithmic dependence on LWP. Table 3 presents the coefficients a and b of the logarithmic function $f(LWP) = a + b \ln(LWP)$ for the temperature θ or the radiation components ΔSR, together with the valid range of these relations for $\theta, \Delta SR$

and LWP. For the values presented in Table 3, our study clearly shows that SLWCs have a positive impact on LWD and LWU, with ΔSR increasing from 0 to 100 W m^{-2} and from 0 to 40 W m^{-2} for LWP ranging from 1.0 to 4.0 and from 1.6 to 2.5 g m^{-2}, respectively. Considering the SR vs. LWP relationship, it seems that we have systematically one of the Gaussian distributions centred around 0 W m^{-2}, reflecting the non-impacting part of SLWCs on SR components. ~~We can note that, whatever the SR considered (Net, LWU, LWD, SWU, SWD), one Gaussian distribution is centred around 0 W m^{-2}, this means SLWCs have no impact on SR.~~

Furthermore, our study also shows that SLWCs have a clear negative impact on SWD and SWU, with ΔSR decreasing from 0 to -140 W m^{-2} and from 0 to -75 W m^{-2} with LWP ranging from 1.2 to 3.8 and from 1.2 to 3.2 g m^{-2}, respectively.

5. Discussion

5.1 Relation with critical temperature

Note that the relationships show an exponential dependence of LWP on both temperature and SR anomaly similar to the dependence of the molar volume and density of water on critical temperature. As a matter of fact, the density ρ (g cm^{-3}) and molar volume ν (cm^{3} mol^{-1}) of liquid water are exponentially varying with temperature (Sippola and Taskinen, 2018):

$$\rho = \rho_0 \exp\{-T_c(A + B\varepsilon + 2C\varepsilon^{1/2})\} \quad (13)$$

$$\nu = \frac{M_{H_2O}}{\rho} = \frac{M_{H_2O}}{\rho_0} \exp\{T_c(A + B\varepsilon + 2C\varepsilon^{1/2})\} \quad (14)$$

where ρ_0 (g cm^{-3}), A (K^{-1}), B (K^{-1}), and C (K^{-1}) are parameters; T_c is the critical temperature whose value varies from 227 to 228 K, and M_{H_2O} (g mol^{-1}) is the molecular weight of water. ε (unitless) is defined as:

$$\varepsilon = \frac{T}{T_c} - 1 \quad (15)$$

where T is temperature in K.

~~5.1. Logarithmic Dependency~~5.2~~1~~. Reference Surface Radiation and sastrugi effect

In order to evaluate the surface radiation in clear-sky conditions at Concordia, we have used, in complement to BSRN observations, and at the closest location to Concordia station, two different data sets of surface radiations from i) the European Center for Medium-Range Weather Forecasts Reanalysis version 5 (ERA5). ERA5 is a climate reanalysis dataset, covering the period 1979 to present. ERA5 is being developed through the Copernicus Climate Change Service (C3S). Extracted data (https://cds.climate.copernicus.eu/cdsapp#!/dataset/reanalysis-era5-single-levels) used here are hourly at a regular horizontal grid of 0.25°x0.25° in clear-sky conditions: surface solar and thermal infrared, downward and net radiations. As explained on the ERA5 website, clear-sky radiations are computed for the same atmospheric conditions of temperature, humidity, ozone, trace gases and aerosol as the corresponding total-sky quantities (clouds included), but assuming that the clouds are not there; ii) the Clouds and the Earth's Radiant Energy System (CERES), containing SYN1deg (Hourly CERES and geostationary (GEO) TOA fluxes, MODIS/VIIRS and GEO cloud properties, MODIS/VIIRS aerosols, and Fu-Liou radiative transfer surface and in-atmospheric (profile) fluxes consistent with the CERES observed TOA fluxes, as explained on https://ceres.larc.nasa.gov/data/). Surface fluxes in SYN1deg are computed with cloud properties derived from MODIS and geostationary satellites (GEO), where each geostationary satellite instrument is calibrated against MODIS (Doelling et al. 2013; 2016) at 1°x1° horizontal resolution (https://ceres.larc.nasa.gov/data/). Aerosol and atmospheric data were included as inputs to calculate the radiation flux.

We have compared the CERES and ERA5 data with the BSRN hourly-averaged data on the 5 reference days (clear-sky conditions) for the Net, LWD, LWU, SWD and SWU SRs. Figure 10 shows these variables for the 26 December 2021. The LWD and LWU values show an overall consistency between ERA5 and CERES (of the order of ~10 W m-2), while a systematic negative bias of ~20-40 W m-2 is observed with respect to BSRN data. However, the net longwave radiation, i.e. the difference LWD – LWU for each data set, is reduced to around 5 W m^{-2}. The SWD and SWU signals from ERA5, CERES and BSRN show a similar diurnal variation with differences less than 50 W m^{-2}. When considering the Net SR, some obvious differences up to 50 W m^{-2} can be seen between BSRN, ERA5 and CERES. Since the net longwave radiation is within 10 W m^{-2} for the three data sets, the source of this difference therefore should come from either SWD or SWU radiation. We have calculated, for BSRN, ERA5 and CERES data, the albedo defined as::

$$albedo = \frac{SWU}{SWD} \tag{10}$$

Figure 11 shows the diurnal evolution of the albedo on 26 December 2021 (clear-sky day). The CERES and ERA5 albedos do not show any significant diurnal variation with quite constant values of 0.74 and 0.83, respectively, whilst the observed BSRN albedo shows a clear diurnal signal with a maximum of 0.85 from 10:00 to 14:00 UTC (from 18:00 to 22:00 LT) and a minimum of 0.70 from 19:00 to 23:00 UTC (from 03:00 to 07:00 LT). The large diurnal signal present in the observed albedo is likely the signature of the sastrugi effect that is obviously absent in the ERA5 and CERES data sets. The BSRN SWU sensor has a circular footprint. For a sensor installed at a height *h* above the ground, 90% of the signal comes from an area at the surface closer than 3.1 *h* (Kassianov et al., 2014). Since at Dome-C the instrument is installed at a height of 2-3 m, the albedo is thus determined by the surface elements in the immediate vicinity (a few meters) of the sensor.

Sastrugi (Figure 12) are features formed by erosion of snow by wind. They are found in polar regions, and in snowy, wind-swept areas of temperate regions, such as frozen lakes or mountain ridges. Sastrugi are distinguished by upwind-facing points, resembling anvils, which move downwind as the surface erodes.

We have fitted the BSRN albedo averaged over the 5 reference days with the sum of 2 sine functions, imposing periods of 24 and 12 hours. Figure 13 shows the BSRN albedo averaged over the five clear-sky days, the fitted trigonometric function and the residuals between the averaged albedo and the fitted function. We can state that the sastrugi effect on the observed clear-sky albedo at Concordia is successfully fitted by 2 sine functions of 24h and 12h periods to within 0.003 mean absolute error, with a coefficient of determination R^2 equal to 0.993 and a root mean square error of 0.0004.

If we suppose that the sastrugi effect impacts mostly SWU rather than SWD, and the albedo calculated from BSRN observations is the "truth", we can calculate a modified SWU* (including the sastrugi effect) for the ERA5 and CERES as:

$$SWU(ERA5)^* = SWD(ERA5) \times albedo(BSRN) \quad (11)$$

$$SWU(CERES)^* = SWD(CERES) \times albedo(BSRN) \quad (12)$$

Then we calculate the modified Net SR* (including the sastrugi effect) considering SWU* for ERA5 and CERES. As an example, we present Figure 14, similar to Figure 10, in which we added the albedo and the SWU* and Net SRs* (including the sastrugi effect) for CERES and ERA5 (solid lines). We observe that the Net SR* for ERA5 and CERES now coincides with the BSRN Net SR to within 5 W m^{-2}, compared to differences up to 50 W m^{-2} found when the sastrugi effect was not taken into account.

Moreover, we have considered all the BSRN observations in Decembers 2018, 2019, 2020 and 2021 to calculate the albedo (Figure 15), and we have superimposed the fitted trigonometric function as described in Figure 13. The presence of clouds is well highlighted by observations that depart from the fitted function whilst, during periods of clear-sky conditions, BSRN albedos coincide well with the fitted function.

The study we have performed was extremely fruitful to evaluate the impact of the SLW clouds on the SR. The methodology requires reference clear-sky SR values that can be evaluated from: 1) models, 2) analyses and 3) observations. Our study has mainly shown that, at the Concordia station, sastrugi were present and strongly impacted the net SR via the surface albedo. This very local phenomenon cannot be taken into account by either the global-scale analyses (ERA5 and CERES), or standard radiative transfer models (e.g. RRTMG). As a consequence, the methodology we have developed based on field observations is likely the most powerful tool to estimate the Net SR in Concordia. It has some drawbacks, as for instance some biases for LWD and LWU between analyses and observations, but the LWD and LWU difference used to calculate the Net SR dramatically lessens the bias.

5.~~2~~3. Modelling SLWC

Previous studies have already underlined the difficulty to model the SLWC together with its impact on surface radiations. Modelling SLWCs over Antarctica is challenging because 1) operational observations ~~from meteorological radiosondes~~ are scarce since the majority of meteorological radiosondes are released from ground stations ~~are~~ located at the coast and very few of them are maintained all year long, and satellite observations are limited to 60°S in geostationary orbit whilst, in polar orbit, the number of available orbits does not exceed 15 per day, and 2) the model should provide a partition function favouring liquid water at the expense of ice for temperatures between -36°C and 0°C in order to calculate realistic SLW ~~concentrations~~contents. Differences of 20 to 50 W m^{-2} in the Net SR were found in the Arpege model (Pailleux et al., 2015) between clouds made of ice or liquid water during the summer 2018-2019 (Ricaud et al., 2020), differences that are very consistent with the results obtained in the present study. Although SLWCs are less present over the Antarctic Plateau than over the coastal region, their radiative impact is not negligible and should be taken into account with great care in order to estimate the radiative budget of the Antarctic continent in one hand, and, on the other hand, over the entire Earth.

5.~~3~~4. Errors

Measurements of temperature, LWP, depolarization signal and SR are altered by random and systematic errors that may affect the relationships we have obtained between LWP and either temperature or SR anomalies. The temperature measured by HAMSTRAD below 1 km has been evaluated against radiosonde coincident observations from 2009 to 2014 (Ricaud et al., 2015) and the resulting bias is 0-2°C below 100 m and between -2 and 0°C between 100 and 1000 m. SLWCs are usually located around 400-600 m above the ground where the cold bias can be estimated to be about -1.0°C. The one-sigma (1-σ) ~~root mean square (~~RMS~~)~~ temperature error over a 7-min integration time is 0.25°C in the PBL and 0.5°C in the free troposphere (Ricaud et al., 2015). As a consequence, given the number of points used in the statistical analysis (>1000), the random error on the weighted-average temperature is negligible (<0.02°C). The LWP random and systematic errors are difficult to evaluate since there is no coincident external data to compare with. Nevertheless, the 1-σ RMS error over a 7-min integration time can be estimated to be 0.25 g m^{-2} giving a random error on the weighted average LWP less than 0.08 g m^{-2}. Based on clear-sky observations, the positive bias can be estimated to be less than 0.4 g m^{-2}. Theoretically, SLW should not exist at temperatures less than -39°C although it has been observed in recent laboratory measurements down to -42.55°C (Goy et al., 2018). Using equation (8) with an LWP bias of 0.4 g m^{-2} gives a temperature of -39.8°C (~0.8°C lower than the theoretical limit of -39°C), so the biases estimated for temperature and LWP are very consistent with theory.

The estimation of systematic and random errors on LIDAR backscattering and depolarization signals and their impact on the attribution/selection of SLWC is not trivial. But the most important point is to evaluate whether the observed cloud is constituted of purely liquid or mixed-phase water. Even considering the backscatter intensity only, we could not exclude that ice particles could have been present in the SLWC events investigated in 2018 (Ricaud et al., 2020). Therefore, in the present analysis, although we made a great attention to diagnose ice in the LIDAR cloud observations, we cannot totally exclude ice particles thus mixed-phase parcels were actually present when we labelled the observed cloud as SLWCs.

The 4 instruments providing LWD, LWU, SWD and SWU SR follow the rules of acquisition, quality check and quality control of the BSRN (Driemel et al., 2018). These data are often considered as a reference against which products based on satellite observations and radiative transfer models (such as e.g. CERES) are validated (Kratz et al., 2020). In polar regions (Lanconelli et al., 2011), the global SWU and SWD SRs are expected to be affected by random errors up to ±20 W m^{-2} while LWD SRs are expected to be affected by random errors not greater than ±10 W m^{-2} (Ohmura et al., 1998). As a consequence, given the large number of observations used per 5 W m^{-2}-wide bins (1000-3000), the random error on the weighted-average SRs is negligible (0.3-0.7 W m^{-2}) whatever the radiations considered, LW and SW.

Finally, apart from the instrument-related SR_{Ref} error, another source of error comes from 1) the geometry of observation and 2) the discontinuous SLWC layer. Firstly, LIDAR is almost zenith pointing, HAMSTRAD makes a scan in the East direction (from 10° elevation to zenith), whilst the BSRN radiometers detect the radiation in a 2π-steradians field of view (3D configuration). That is to say, in our analysis, the whole sky contributes to the radiation whilst only the cloud at zenith (1D configuration) and on the East direction (2D configuration) is observed by the LIDAR and HAMSTRAD, respectively. Secondly, SLWCs cannot be considered as uniform in the whole (see e.g. broken cloud fields in Figure 2).

5.54. Other clouds

Although the method we have developed to select the SLWCs has been validated using the amount of LWP and, in another study, using space-borne observations (Ricaud et al., 2020), we cannot rule out that, associated with the SLW droplets, are also ice particles, that is clouds are constituted of a mixture of liquid and solid water. Generally, such clouds are a superposition of a lower layer being made of liquid water and an upper layer being made of solid water (see Fig. 12.3 from Lamb and Verlinde, 2011). These mixed-layer clouds do not significantly modify the relationship between temperature and LWP because 1) SLW observations from HAMSTRAD are only sensitive to water in liquid phase and 2) temperature from HAMSTRAD is selected at times and vertical heights where the LIDAR depolarization signal is very low (<5%). Although we have verified that pure ice clouds were not selected by our method, we cannot differentiate mixed-phase clouds from purely SLWCs. As a consequence, the presence of mixed-phase~~d~~ clouds in addition to SLWCs may explain ~~in our results~~ the negative part of the Net, LWD and LWU ΔSR ([-20;0] W m^{-2}) and the positive part of the SWD and SWU ΔSR ([0;10] W m^{-2}) for low values of LWP ([0.8;1.6] g m^{-2}).~~As a consequence, the relationship between ΔSR and LWP might be affected by the presence of mixed-phased clouds in addition to SLWCs. This may explain the negative part of the Net, LWD and LWU ΔSR ([−20; 0] W m^{-2}) and the positive part of the SWD and SWU ΔSR ([0; 10] W m^{-2}) for low values of LWP ([0.8; 1.6] g m^{-2}).~~

Furthermore, we already have noticed that SLWCs developed at the top of the PBL (Ricaud et al., 2020) in the “entrainment zone” and maintained in the “capping inversion zone”, following the terminology of Stull (1988), at a height ranging from 100 to 1000 m above ground level. Nevertheless, during the local “night” at 00:00-06:00 LT, the PBL may collapse down to a very low height ranging 20-50 m. In this configuration, it is hard to differentiate from LIDAR observations between a SLWC and a fog episode, although the LIDAR can measure depolarization (but not backscatter) down to approximately 10-30 m above the ground (Figure S3 in Chen et al., 2017), so that we can distinguish liquid/frozen clouds very close to the ground.

Finally, we cannot rule out that, above the SLWCs that are actually observed by both LIDAR and HAMSTRAD, other clouds might be present, as e.g. cirrus clouds constituted of ice crystals. These mid-to-upper tropospheric clouds cannot be detected by HAMSTRAD (no sensitivity to ice crystals). In the presence of SLWCs either low in altitude or optically thick, the LIDAR backscatter signal is decreased in order to avoid saturation and the signal from upper layers is thus almost cancelled. These mid-to-high-altitude clouds are observed by the BSRN instruments and SR can be affected in this configuration. Based on the presence of cirrus clouds before or after the SLWCs (and sometimes during the SLWCs if optically thin), we can estimate that the number of days when SLWCs and cirrus clouds are simultaneously present to cover less than 10% of our period of interest.

5.~~5~~6. Potential radiative impact of SLWCs over Antarctica

Based on 2007-2010 reanalyses, observations and climate models (Lenaerts et al., 2017), LWP over Antarctica is on average less than 10 g m^{-2}, with slightly larger values in summer than in winter by 2-5 g m^{-2}. Over Western Antarctica, LWPs are larger (20-40 g m^{-2}) than over Eastern Antarctica (0-10 g m^{-2}). As a consequence, LWPs observed at Concordia ~~is~~are consistent with values observed over the Eastern Plateau, with a factor 2-4 smaller than th~~at~~ose observed over the Western continent. Based on our results and on the observed cloud fraction (η_{CF}) of SLWCs over Antarctica for different seasons (Listowski et al., 2019), we have estimated the potential radiative impact of SLWCs at the scale of the Antarctic continent ($Net\ \Delta SR^{max}_{global}$) from the maximum of $Net\ \Delta SR$ ($Net\ \Delta SR^{max} = 50$ W m^{-2}) computed in our study:

$$Net\ \Delta SR^{max}_{global} = \eta_{CF} \times\ Net\ \Delta SR^{max} \tag{13}$$

In summer, η_{CF} is varying from 5% in Eastern Antarctica to 40% in Western Antarctica whilst, in winter, it is varying from 0% in Eastern Antarctica to 20% in Western Antarctica (Listowski et al., 2019). In December, if we consider η_{CF} for SLW-containing cloud (that is to say both mixed-phase cloud and unglaciated SLW cloud consistent with our study), we find for a lower-level altitude cut-off of 0, 500 and 1000 m (Figure B1 in Listowski et al., 2019), a potential radiative impact $Net\ \Delta SR^{max}_{global}$ over Antarctica of 9, 7 and 5 W m^{-2}, respectively. We now separate the Eastern elevated Antarctic Plateau from the Western Antarctica (Figure 5 in Listowski et al., 2019) for the 4 seasons. Over Eastern Antarctica, we find that $Net\ \Delta SR_{global}^{max} =$ 0.5-5.0 W m^{-2} in December-January-February (DJF) and 0-2.5 W m^{-2} for the remaining seasons. Over Western Antarctica, the potential radiative impact is much more intense because of higher temperatures and lower elevations compared to the Eastern Antarctic Plateau: $Net\ \Delta SR_{global}^{max} =$ 12.5-30.0 W m^{-2} in DJF (30 W m^{-2} over the Antarctica Peninsula); 7.5-20.0 W m^{-2} in March-April-May; 2.5-10.0 W m^{-2} in June-July-August; and 5.0-12.5 W m^{-2} in September-October-November.

6. Conclusions

Combining the observations of temperature, water vapour and liquid water path from a ground-based microwave radiometer, backscattering and depolarization from a ground-based LIDAR and surface radiations at long and short wavelengths, our analysis has been able to evaluate the presence of supercooled liquid water clouds over the Dome C station in summer. Focu~~s~~sing on ~~4~~ the month of December~~s~~ in ~~(~~2018-2021~~)~~, we established that in~~the sensitivity of the~~ SLWCs ~~to~~ temperature ~~and LWP has been established with temperature~~ logarithmically increases~~ing~~ from -36.0°C to -16.0°C when ~~liquid water path~~LWP increases from 1.0 to 14.0 g m^{-2}. We have also evaluated that SLWCs positively affect the net ~~surface radiation~~SR, which logarithmically increases from 0.0 to 50.0 W m^{-2} when ~~liquid water path~~LWP increases from 1.7 to 3.0 g m^{-2}. Our study clearly shows that: 1) SLWCs have a positive impact on LWD and LWU, with ΔSR increasing from 0 to 100 W m^{-2} and from 0 to 40 W m^{-2} for LWP ranging from 1.0 to 4.0 and from 1.6 to 2.5 g m^{-2}, respectively, and 2) SLWCs have a clear negative impact on SWD and SWU, with ΔSR decreasing from 0 to -140 W m^{-2} and from 0 to -75 W m^{-2} with LWP ranging from 1.2 to 3.8 and from 1.2 to 3.2 g m^{-2}, respectively.

Our study has ~~mainly~~ shown that, at the Concordia station, sastrugi were present and strongly impacted the ~~SWU signal,~~ net SR via the surface albedo~~thus the albedo, thus the Net SR~~. This very local phenomenon cannot be taken into account by ~~n~~either ~~by~~ the global-scale analyses (ERA5 and CERES), ~~n~~or ~~by~~ standard radiative transfer models. As a consequence, the methodology we have developed based on ~~real~~field observations is ~~probably~~likely the most powerful tool to estimate the Net SR in Concordia. It has some drawbacks, as for instance some biases for LWD and LWU between analyses and observations, but the LWD – LWU difference that is used to calculate the Net SR dramatically lessens the bias.

Finally, extrapolating the radiative impact of the SLWCs from the Dome C station to the Antarctic continent shows that SLWCs have a great potential radiative impact all over Antarctica whatever the season considered, up to 5.0 W m^{-2} over the Eastern Antarctic Plateau and up to 30 W m^{-2} over the Antarctic Peninsula in ~~DJF~~summer season. This stresses the importance of accurately modelling SLWCs when calculating the Earth energy budget to adequately forecast the Earth climate evolution, especially since the climate is rapidly changing in Antarctica, as illustrated by the surface temperature record of -12°C recently observed in March 2022 at the Concordia station and largely publicized worldwide (see e.g. https://www.9news.com.au/world/antarctica-heatwave-extreme-warm-weather-recorded-concordia-research-station/3364dd91-2051-4df5-8cfc-5f2819058604).

Data availability

HAMSTRAD data are available at http://www.cnrm.meteo.fr/spip.php?article961&lang=en (last access: 3 May 2022). The tropospheric depolarization LIDAR data are reachable at http://lidarmax.altervista.org/lidar/home.php (last access: 3 May 2022). Radiosondes are available at http://www.climantartide.it (last access: 3 May 2022). BSRN data can be obtained from the ftp server (https://bsrn.awi.de/data/data-retrieval-via-ftp/) (last access: 3 May 2022).

Author contribution

PR, MDG, and AL provided the observational data. PR developed the methodology. All the co-authors participated in the data analysis and in the data interpretation. PR prepared the manuscript with contributions from all co-authors.

Competing interests

The authors declare that they have no conflict of interest.

Acknowledgments

The present research project Water Budget over Dome C (H2O-DC) has been approved by the Year of Polar Prediction (YOPP) international committee. The HAMSTRAD programme (910) was supported by the French Polar Institute, Institut polaire français Paul-Emile Victor (IPEV), the Institut National des Sciences de l'Univers (INSU)/Centre National de la Recherche Scientifique (CNRS), Météo-France and the Centre National d'Etudes Spatiales (CNES). The permanently manned Concordia station is jointly operated by IPEV and the Italian Programma Nazionale Ricerche in Antartide (PNRA). The tropospheric LIDAR operates at Dome C from 2008 within the framework of several Italian national (PNRA) projects. We would like to thank all the winterover personnel who worked at Dome C on the different projects: HAMSTRAD, aerosol LIDAR and BSRN. We would like to thank the two anonymous reviewers for their beneficial comments.

References

Bergeron, T., 1928: Über die dreidimensional verknüpfende Wetteranalyse. – Geophys. Norv.

Bromwich, D. H., Nicolas, J. P., Hines, K. M., Kay, J. E., Key, E. L., Lazzara, Lubin, D., McFarquhar, G. M., Gorodetskaya, I. V., Grosvenor, D. P., Lachlan-Cope, T., and van Lipzig, N. P. M.: Tropospheric clouds in Antarctica, Rev. Geophys., 50, RG1004, https://doi.org/10.1029/2011RG000363, 2012.

Bromwich, D. H., Otieno, F. O., Hines, K. M., Manning, K. W., and Shilo, E.: Comprehensive evaluation of polar weather research and forecasting model performance in the Antarctic, J. Geophys. Res.-Atmos., 118, 274–292, 2013.

Chen, X., Virkkula, A., Kerminen, V.-M., Manninen, H. E., Busetto, M., Lanconelli, C., Lupi, A., Vitale, V., Del Guasta, M., Grigioni, P., Väänänen, R., Duplissy, E.-M., Petäjä, T., and Kulmala, M.: Features in air ions measured by an air ion spectrometer (AIS) at Dome C, Atmos. Chem. Phys., 17, 13783–13800, https://doi.org/10.5194/acp-17-13783-2017, 2017.

Clough, S. A., M. W. Shephard, E. J. Mlawer, J.S. Delamere, M. J. Iacono, K. Cady-Pereira, S. Boukabara, and P. D. Brown. Atmospheric radiative transfer modeling: A summary of the aer codes. J. Quant. Spectrosc. Radiat. Transfer, 91:233–244, 2005.

Doelling, D. R., N. G. Loeb, D. F. Keyes, M. L. Nordeen, D. Morstad, C. Nguyen, B. A. Wielicki, D. F. Young, M. Sun, 2013: Geostationary Enhanced Temporal Interpolation for CERES Flux Products, Journal of Atmospheric and Oceanic Technology, 30(6), 1072-1090. doi: 10.1175/JTECH-D-12-00136.1.

Doelling, D. R., M. Sun, L. T. Nguyen, M. L. Nordeen, C. O. Haney, D. F. Keyes, P. E. Mlynczak, 2016: Advances in Geostationary-Derived Longwave Fluxes for the CERES Synoptic (SYN1deg) Product, Journal of Atmospheric and Oceanic Technology, 33(3), 503-521. doi: 10.1175/JTECH-D-15-0147.1.

Driemel, A., Augustine, J., Behrens, K., Colle, S., Cox, C., Cuevas-Agulló, E., Denn, F. M., Duprat, T., Fukuda, M., Grobe, H., Haeffelin, M., Hodges, G., Hyett, N., Ijima, O., Kallis, A., Knap, W., Kustov, V., Long, C. N., Longenecker, D., Lupi, A., Maturilli, M., Mimouni, M., Ntsangwane, L., Ogihara, H., Olano, X., Olefs, M., Omori, M., Passamani, L., Pereira, E. B., Schmithüsen, H., Schumacher, S., Sieger, R., Tamlyn, J., Vogt, R., Vuilleumier, L., Xia, X., Ohmura, A., and König-Langlo, G.: Baseline Surface Radiation Network (BSRN): structure and data description (1992–2017), Earth Syst. Sci. Data, 10, 1491–1501, https://doi.org/10.5194/essd-10-1491-2018, 2018.

Findeisen, W., 1938: Kolloid-meteorologische Vorgänge bei Niederschlagsbildung. Meteorol. Z. 55, 121–133. (translated and edited by Volken, E., A.M. Giesche, S. Brönnimann. – Meteorol. Z. 24 (2015), DOI:10.1127/metz/2015/0675).

Goy, C., Potenza, M. A., Dedera, S., Tomut, M., Guillerm, E., Kalinin, A., Voss, K.-O., Schottelius, A., Petridis, N., Prosvetov, A., Tejeda, G., Fernández, J. M., Trautmann, C., Caupin, F., Glasmacher, U., and Grisenti, R. E.: Shrinking of rapidly evaporating water microdroplets reveals their extreme supercooling, Phys. Rev. Lett., 120, 015501, https://doi.org/10.1103/PhysRevLett.120.015501, 2018.

Grazioli, J., Genthon, C., Boudevillain, B., Duran-Alarcon, C., Del Guasta, M., Madeleine, J.-B., and Berne, A.: Measurements of precipitation in Dumont d'Urville, Adélie Land, East Antarctica, The Cryosphere, 11, 1797–1811, https://doi.org/10.5194/tc-11-1797-2017, 2017.

Grosvenor, D. P., Choularton, T. W., Lachlan-Cope, T., Gallagher, M. W., Crosier, J., Bower, K. N., Ladkin, R. S., and Dorsey, J. R.: In-situ aircraft observations of ice concentrations within clouds over the Antarctic Peninsula and Larsen Ice Shelf, Atmos. Chem. Phys., 12, 11275–11294, https://doi.org/10.5194/acp-12-11275-2012, 2012.

Hogan, R. J. and Illingworth, A. J.: The effect of specular reflection on spaceborne lidar measurements of ice clouds, Report of the ESA Retrieval algorithm for EarthCARE project, 5 pp., 2003.

Kassianov E, Barnard J, Flynn C, Riihimaki L, Michalsky J, Hodges G (2014) Areal-averaged spectral surface albedo from ground-based transmission data alone: toward an operational retrieval. Atmosphere 5:597–621. https://doi.org/10.3390/atmos503059)

King, J. C., Argentini, S. A., and Anderson, P. S.: Contrasts between the summertime surface energy balance and boundary layer structure at Dome C and Halley stations, Antarctica, J. Geophys. Res.-Atmos., 111, D02105, https://doi.org/10.1029/2005JD006130, 2006.

King, J. C., Gadian, A., Kirchgaessner, A., Kuipers Munneke, P., Lachlan-Cope, T. A., Orr, A., Reijmer, C., Broeke, M. R., van Wessem, J. M., and Weeks, M.: Validation of the summertime surface energy budget of Larsen C Ice Shelf (Antarctica) as represented in three high-resolution atmospheric models, J. Geophys. Res.-Atmos., 120, 1335–1347, https://doi.org/10.1002/2014JD022604, 2015.

Kratz, D. P., Gupta, S. K., Wilber, A. C., and Sothcott, V. E.: Validation of the CERES Edition-4A Surface-Only Flux Algorithms, J. Appl. Meteorol. Clim., 59, 281–295, https://doi.org/10.1175/JAMC-D-19-0068.1, 2020.

Lachlan-Cope, T.: Antarctic clouds, Polar Res., 29, 150–158, 2010.

Lachlan-Cope, T., Listowski, C., and O'Shea, S.: The microphysics of clouds over the Antarctic Peninsula – Part 1: Observations, Atmos. Chem. Phys., 16, 15605–15617, https://doi.org/10.5194/acp-16-15605-2016, 2016.

Lamb, D., and J. Verlinde: Physics and chemistry of clouds. Cambridge University Press, 2011.

Lanconelli, C., Busetto, M., Dutton, E. G., König-Langlo, G., Maturilli, M., Sieger, R., Vitale, V., and Yamanouchi, T.: Polar baseline surface radiation measurements during the International Polar Year 2007–2009, Earth Syst. Sci. Data, 3, 1–8, https://doi.org/10.5194/essd-3-1-2011, 2011.

Lawson, R. P. and Gettelman, A.: Impact of Antarctic mixed-phase clouds on climate, P. Natl. Acad. Sci. USA, 111, 18156–18161, 2014.

Legrand, M., Yang, X., Preunkert, S., and Therys, N.: Year-round records of sea salt, gaseous, and particulate inorganic bromine in the atmospheric boundary layer at coastal (Dumont d'Urville) and central (Concordia) East Antarctic sites, J. Geophys. Res. Atmos., 121, 997–1023, https://doi.org/10.1002/2015JD024066, 2016.

Lemus, L., Rikus, L., Martin, C., and Platt, R.: Global cloud liquid water path simulations. J. Climate, 10(1), 52-64, 1997.

Lenaerts, J. T., Van Tricht, K., Lhermitte, S. and L'Ecuyer, T. S.: Polar clouds and radiation in satellite observations, reanalyses, and climate models, Geophysical Research Letters, 44(7), 3355-3364, 2017.

Listowski, C. and Lachlan-Cope, T.: The microphysics of clouds over the Antarctic Peninsula – Part 2: modelling aspects within Polar WRF, Atmos. Chem. Phys., 17, 10195–10221, https://doi.org/10.5194/acp-17-10195-2017, 2017.

Listowski, C., Delanoë, J., Kirchgaessner, A., Lachlan-Cope, T., and King, J.: Antarctic clouds, supercooled liquid water and mixed phase, investigated with DARDAR: geographical and seasonal variations, Atmos. Chem. Phys., 19, 6771–6808, https://doi.org/10.5194/acp-19-6771-2019, 2019.

Lubin, D., Chen, B., Bromwich, D. H., Somerville, R. C., Lee, W. H., and Hines, K. M.: The Impact of Antarctic Cloud Radiative Properties on a GCM Climate Simulation, J. Climate, 11, 447-462, 1998.

Mishchenko, M. I., Hovenier, J. W., and Travis, L. D. (Eds.): Light Scattering by Nonspherical Particles: Theory, Measurements, and Applications, Academic Press, chap. 14, 393–416, 2000.

Ohmura, A., Dutton,E. G., Forgan, B., Fröhlich, C., Gilgen, H., Hegner, H., Heimo, A., König-Langlo, G., McArthur, B., Müller, G., Philipona, R., Pinker, R., Whitlock, C. H., Dehne, K., and Wild, M.: Baseline Surface Radiation Network (BSRN/WCRP): New precision radiometry for climate research, B. Am. Meteorol. Soc., 79(10), 2115-2136, 1998.

O'Shea, S. J., Choularton, T. W., Flynn, M., Bower, K. N., Gallagher, M., Crosier, J., Williams, P., Crawford, I., Flem- ing, Z. L., Listowski, C., Kirchgaessner, A., Ladkin, R. S., and Lachlan-Cope, T.: In situ measurements of cloud microphysics and aerosol over coastal Antarctica during the MAC campaign, Atmos. Chem. Phys., 17, 13049–13070, https://doi.org/10.5194/acp-17-13049-2017, 2017.

Pailleux, J., Geleyn, J.-F., El Khatib, R., Fischer, C., Hamrud, M., Thépaut, J.-N., Rabier, F., Andersson, E., Salmond, D., Burridge, D., Simmons, A., and Courtier, P.: Les 25 ans du système de prévision numérique du temps IFS/Arpège, La Météorologie, 89, 18–27, https://doi.org/10.4267/2042/56594, 2015.

Ricaud, P., Gabard, B., Derrien, S., Chaboureau, J.-P., Rose, T., Mombauer, A. and Czekala, H.: HAMSTRAD-Tropo, A 183-GHz Radiometer Dedicated to Sound Tropospheric Water Vapor Over Concordia Station, Antarctica, IEEE T. Geosci. Remote, 48, 1365–1380, doi: 10.1109/TGRS.2009.2029345, 2010a.

Ricaud, P., Gabard, B., Derrien, S., Attié, J.-L., Rose, T., and Czekala, H.: Validation of tropospheric water vapor as measured by the 183-GHz HAMSTRAD Radiometer over the Pyrenees Mountains, France, IEEE T. Geosci. Remote, 48, 2189–2203, 2010b.

Ricaud, P., Genthon, C., Durand, P., Attié, J.-L., Carminati, F., Canut, G., Vanacker, J.-F., Moggio, L., Courcoux, Y., Pellegrini, A., and Rose, T.: Summer to Winter Diurnal Variabilities of Temperature and Water Vapor in the lowermost troposphere as observed by the HAMSTRAD Radiometer over Dome C, Antarctica, Bound.-Lay. Meteorol., 143, 227–259, doi:10.1007/s10546-011-9673-6, 2012.

Ricaud, P., Grigioni, P., Zbinden, R., Attié, J.-L., Genoni, L., Galeandro, A., Moggio, A., Montaguti, S., Petenko, I., and Legovini, P.: Review of tropospheric temperature, absolute humidity and integrated water vapour from the HAMSTRAD radiometer installed at Dome C, Antarctica, 2009–14, Antarct. Sci., 27, 598-616, doi:10.1017/S0954102015000334, 2015.

Ricaud, P., Bazile, E., del Guasta, M., Lanconelli, C., Grigioni, P., and Mahjoub, A.: Genesis of diamond dust, ice fog and thick cloud episodes observed and modelled above Dome C, Antarctica, Atmos. Chem. Phys., 17, 5221-5237, https://doi.org/10.5194/acp-17-5221-2017, 2017.

Ricaud, P., Del Guasta, M., Bazile, E., Azouz, N., Lupi, A., Durand, P., Attié, J.-L., Veron, D., Guidard, V., and Grigioni, P.: Supercooled liquid water cloud observed, analysed, and modelled at the top of the planetary boundary layer above Dome C, Antarctica, Atmos. Chem. Phys., 20, 4167–4191, https://doi.org/10.5194/acp-20-4167-2020, 2020.

Sippola, H., and Taskinen, P.: Activity of supercooled water on the ice curve and other thermodynamic properties of liquid water up to the boiling point at standard pressure, J. Chem. Engineer. Data, 63(8), 2986-2998, 2018.

Storelvmo, T. and Tan, I.: The Wegener–Bergeron–Findeisen process—Its discovery and vital importance for weather and climate, Meteor. Z, 24, 455-461, 2015.

Stull, R. B.: An introduction to boundary layer meteorology, ~~Vol. 13, Springer Science & Business Media,~~ Kluwer Academic Publisher, ~~2012~~1988.

Tomasi, C., Petkov, B., Mazzola, M., Ritter, C., di Sarra, A., di Iorio, T., and del Guasta, M.: Seasonal variations of the relative optical air mass function for background aerosol and thin cirrus clouds at Arctic and Antarctic sites, Remote Sensing, 7(6), 7157-7180, 2015.

Wegener, A. 1911. Thermodynamik der Atmosphäre. – Leipzig, Germany: Barth.

Wille, J. D., Favier, V., Dufour, A., Gorodetskaya, I. V., Turner, J., Agosta, C. and Codron, F.: West Antarctic surface melt triggered by atmospheric rivers, Nature Geoscience, 12(11), 911-916, 2019.

Young, G., Lachlan-Cope, T., O'Shea, S. J., Dearden, C., Listowski, C., Bower, K. N., Choularton, T. W., and Gallagher, M. W.: Radiative effects of secondary ice enhancement in coastal Antarctic clouds, Geophys. Res. Lett., 46, 2312–2321, https://doi.org/10.1029/2018GL080551, 2019.

Tables

Table 1. Time-coincident data availability (green) in Decembers 2018-2021 for HAMSTRAD temperature and LWP, Lidar Backscattering and Depolarization and BSRN Surface Radiances (Net, LWD, LWU, SWD and SWU). The 5 clear-sky (Reference) days are highlighted in red.

Year	December Days																														
	1	2	3	4	5	6	7	8	9	10	11	12	13	14	15	16	17	18	19	20	21	22	23	24	25	26	27	28	29	30	31
2018																															
2019																															
2020																															
2021																															

Table 2. Gaussian functions fitted to the $N(x)$ function for $x = \theta$ (°C) or ΔSR (W m^{-2}). Units of a_1, a_2, a_3, and c are in count number for θ and ΔSR; units of μ_1, μ_2, μ_3, σ_1, σ_2, and σ_3 are in °C for θ and in W m^{-2} for ΔSR.

x	a_1	μ_1	σ_1	a_2	μ_2	σ_2	a_3	μ_3	σ_3	c
$\boldsymbol{\theta}$	15.0 10^3	-31.5	1.45	5.0 10^3	-28.0	1.65	0.5 10^3	-19.0	2.5	-9.1 10^{-6}
Net ΔSR	2106.5	0.02	19.2	941.4	29.8	22.0	-	-	-	19.5
LWD ΔSR	1010.8	80.1	21.9	1565.6	10.0	23.9	-	-	-	18.4
LWU ΔSR	1476.4	-10.0	14.9	1834.7	25.0	16.2	-	-	-	185.4
SWD ΔSR	1317.2	-5.0	15.8	717.4	-80.0	64.7	-	-	-	9.1
SWU ΔSR	1928.8	-5.0	19.2	1163.4	-59.9	17.6	-	-	-	9.1

Table 3. Coefficients of the relations $f(LWP) = a + b\ln(LWP)$ for the temperature θ or surface radiation anomalies ΔSR. Units of θ and ΔSR, as well as of their corresponding "*a*" values are in °C and W m^{-2}, respectively; units of *b* are in °C g^{-1} m^{2} for θ and in W / g for ΔSR; units of LWP are in g m^{-2}. The last column shows the range of LWP values for which the relation is valid (in black), and in red (blue) the sub-range in which a positive (negative) impact is observed on ΔSR. Note that $a \pm \delta a$ corresponds to the range of *a* values where the relationship is valid.

$f(LWP)$	$a \pm \delta a$	b	Valid range for θ or ΔSR	Valid range for LWP
θ	-33.8 $\pm$ 1.5	6.5	$[-36; -16]$	[1.0; 14.0]
Net ΔSR	-50.0 $\pm$ 10.0	90.0	$[-15; 50]$	[1.5; 3.0] / [1.7; 3.0]
LWD ΔSR	5.0 $\pm$ 15.0	65.0	$[-10; 100]$	[0.8; 4.0]/ [1.0; 4.0]
LWU ΔSR	-45.0 $\pm$ 30.0	90.0	$[-20; 40]$	[1.3; 2.5]/ [1.6; 2.5]
SWD ΔSR	30.0 $\pm$ 30.0	-130.0	$[-140; 10]$	[1.1; 3.8]/ [1.2; 3.8]
SWU ΔSR	15.0 $\pm$ 15.0	-75.0	$[-75; 10]$	[1.1; 3.2]/ [1.2; 3.2]

812

Figures

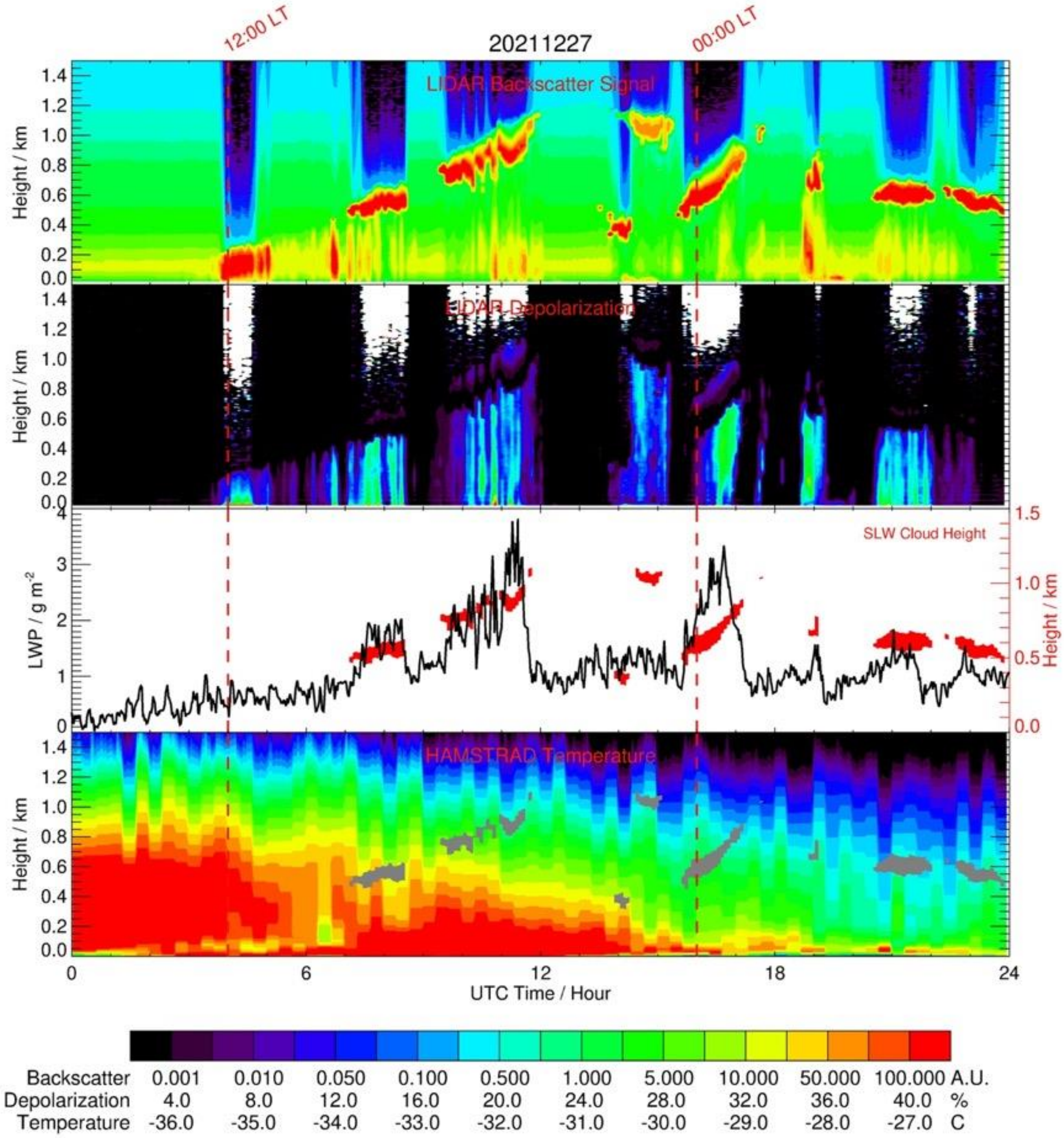
12:00 LT
00:00 LT
20211227
LIDAR Backscatter Signal
LIDAR Depolarization
SLW Cloud Height
HAMSTRAD Temperature
Height / km
LWP / g m-2
UTC Time / Hour
Backscatter 0.001 0.010 0.050 0.100 0.500 1.000 5.000 10.000 50.000 100.000 A.U.
Depolarization 4.0 8.0 12.0 16.0 20.0 24.0 28.0 32.0 36.0 40.0 %
Temperature -36.0 -35.0 -34.0 -33.0 -32.0 -31.0 -30.0 -29.0 -28.0 -27.0 C

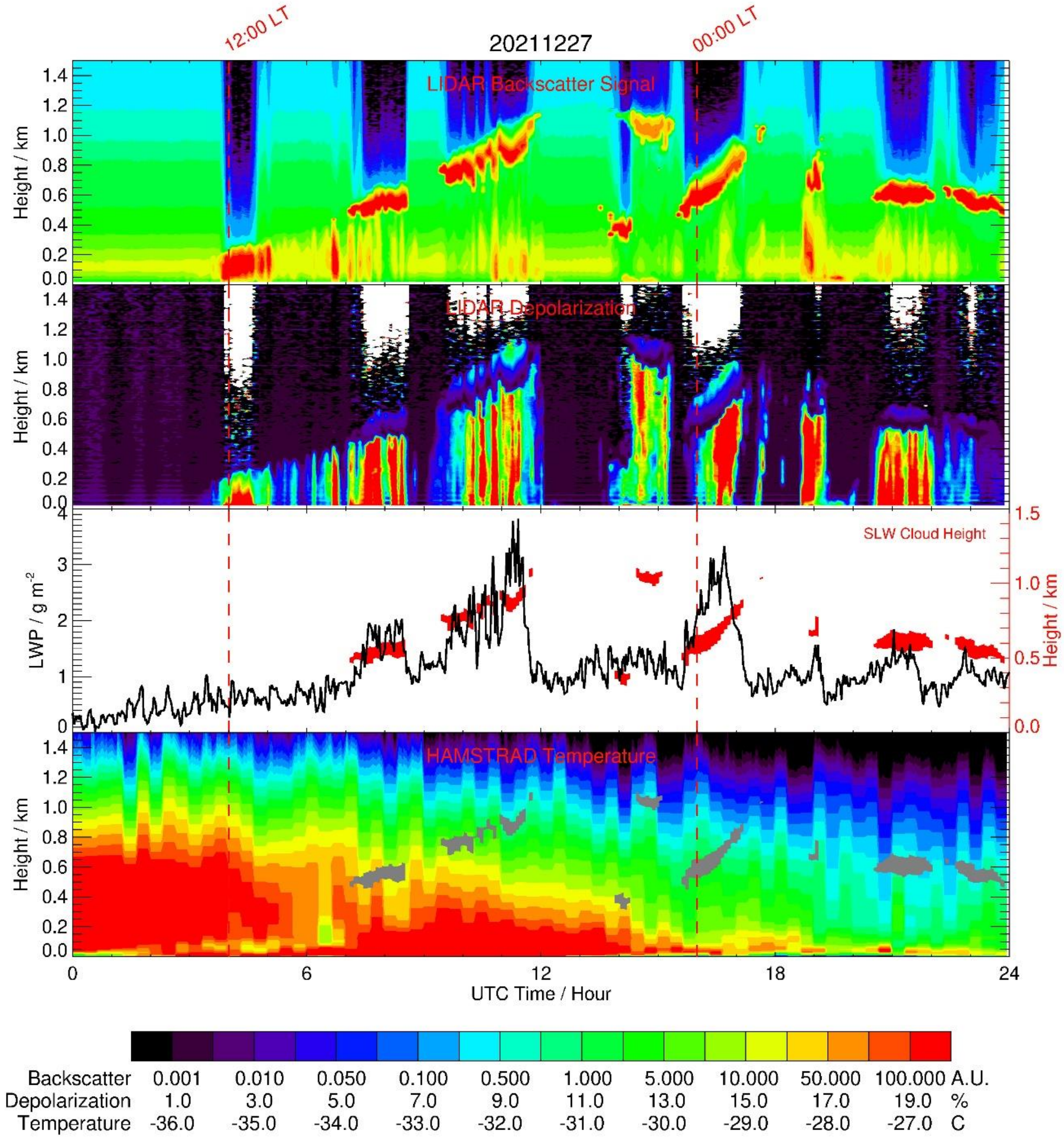

Figure 1: (From top to bottom): Time evolution (UTC, hour) of the Lidar Backscattering Signal, the Lidar Depolarization Signal, the HAMSTRAD LWP and the HAMSTRAD temperature profile measured on 27 December 2021. The time evolution of the SLW cloud (as diagnosed by a backscattering signal > 60 A.U. and a depolarization signal < 5%) is highlighted by the red and grey areas in the third and the forth panel from the top, respectively. The height above the ground is shown on the third panel from the top with the y-axis on the right. The 00:00 and 12:00 local times (LT) are highlighted by 2 vertical dashed lines.

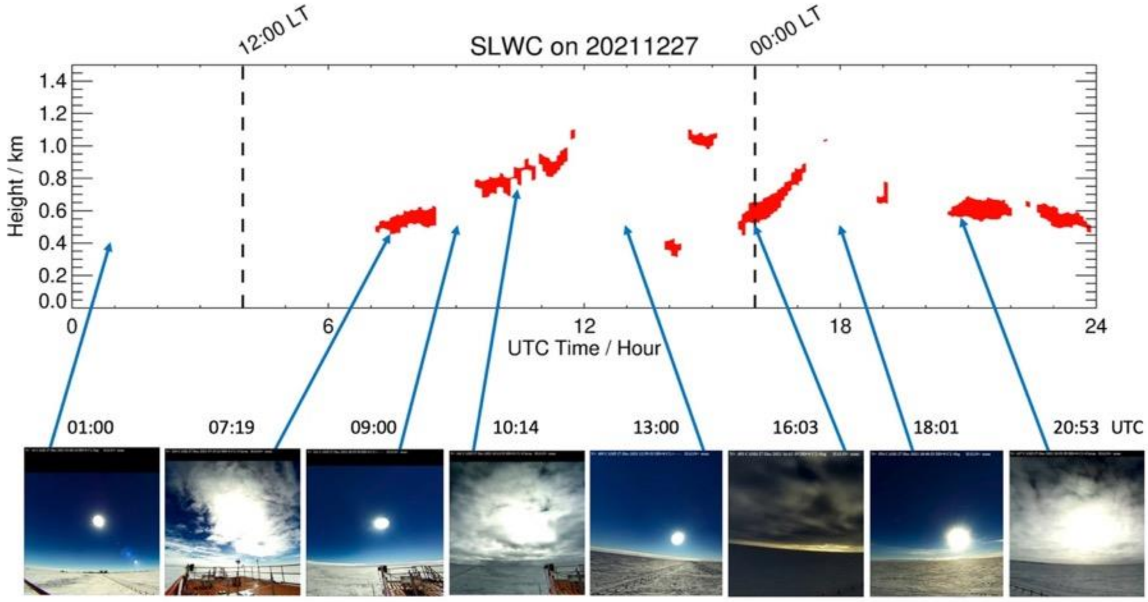

Figure 2: (Top) Time evolution (UTC, hour) of the SLWC (red areas) on 27 December 2021. (Bottom, from left to right) Snapshots from the HALO-CAM video camera taken on: 01:00 (no SLWC), 07:19 (SLWC), 09:00 (no SLWC), 10:14 (SLWC), 13:00 (no SLWC), 16:03 (SLWC), 18:01 (no SLWC) and 20:53 UTC (SLWC). The 00:00 and 12:00 local times (LT) are highlighted by 2 vertical dashed lines.

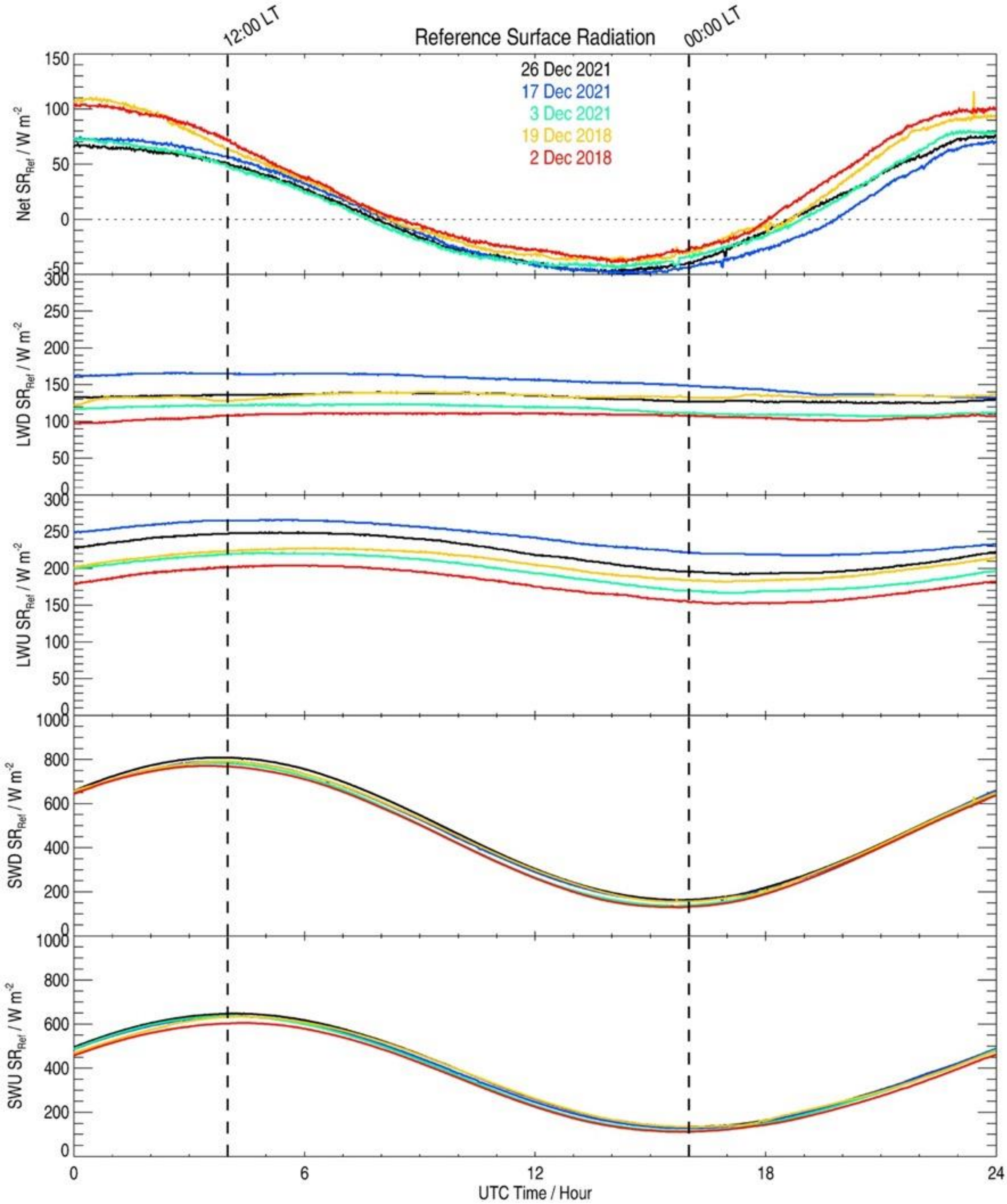

Figure 3: Time evolution (UTC, hour) of the clear-sky surface radiations (SR, W m^{-2}) observed by the BSRN instruments on 2 December 2018 (red), 19 December 2018 (orange), 3 December 2021 (green), 17 December 2021 (blue) and 26 December 2021 (black): (from top to bottom) Net SR, Longwave Downward SR (LWD SR), Longwave Upward SR (LWU SR), Shortwave Downward SR (SWD SR) and Shortwave Upward SR (SWU SR). The 00:00 and 12:00 local times (LT) are highlighted by 2 vertical dashed lines.

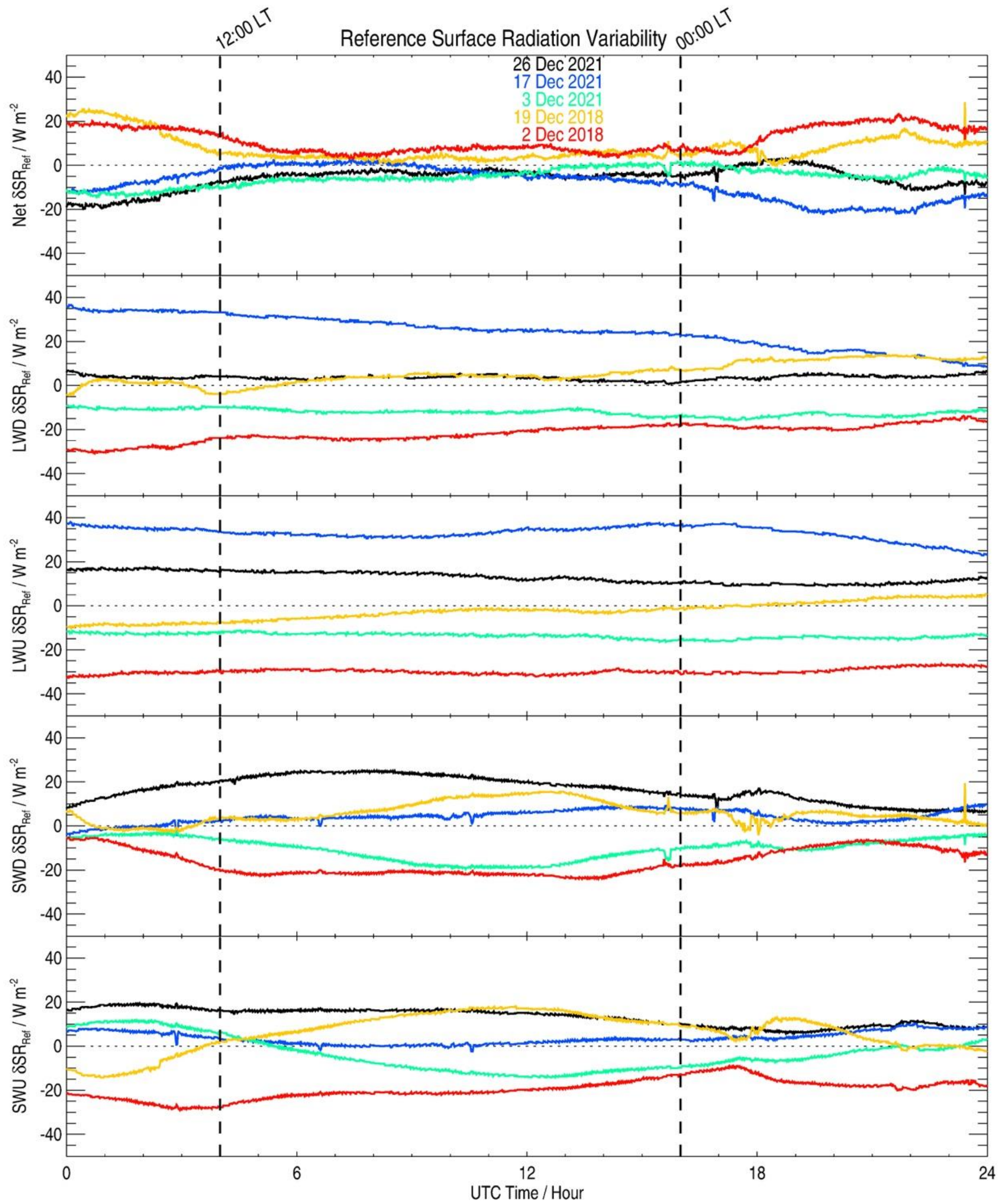

Figure 4: Time evolution (UTC, hour) of the clear-sky surface radiation variability (δSR_{Ref}, W m^{-2}), namely the clear-sky surface radiations observed by the BSRN instruments on 2 December 2018 (red), 19 December 2018 (orange), 3 December 2021 (green), 17 December 2021 (blue) and 26 December 2021 (black) minus the corresponding values averaged over the 5 cloud-free days: (from top to bottom) Net SR, Longwave Downward SR (LWD SR), Longwave Upward

SR (LWU SR), Shortwave Downward SR (SWD SR) and Shortwave Upward SR (SWU SR). The 00:00 and 12:00 local times (LT) are highlighted by 2 vertical dashed lines.

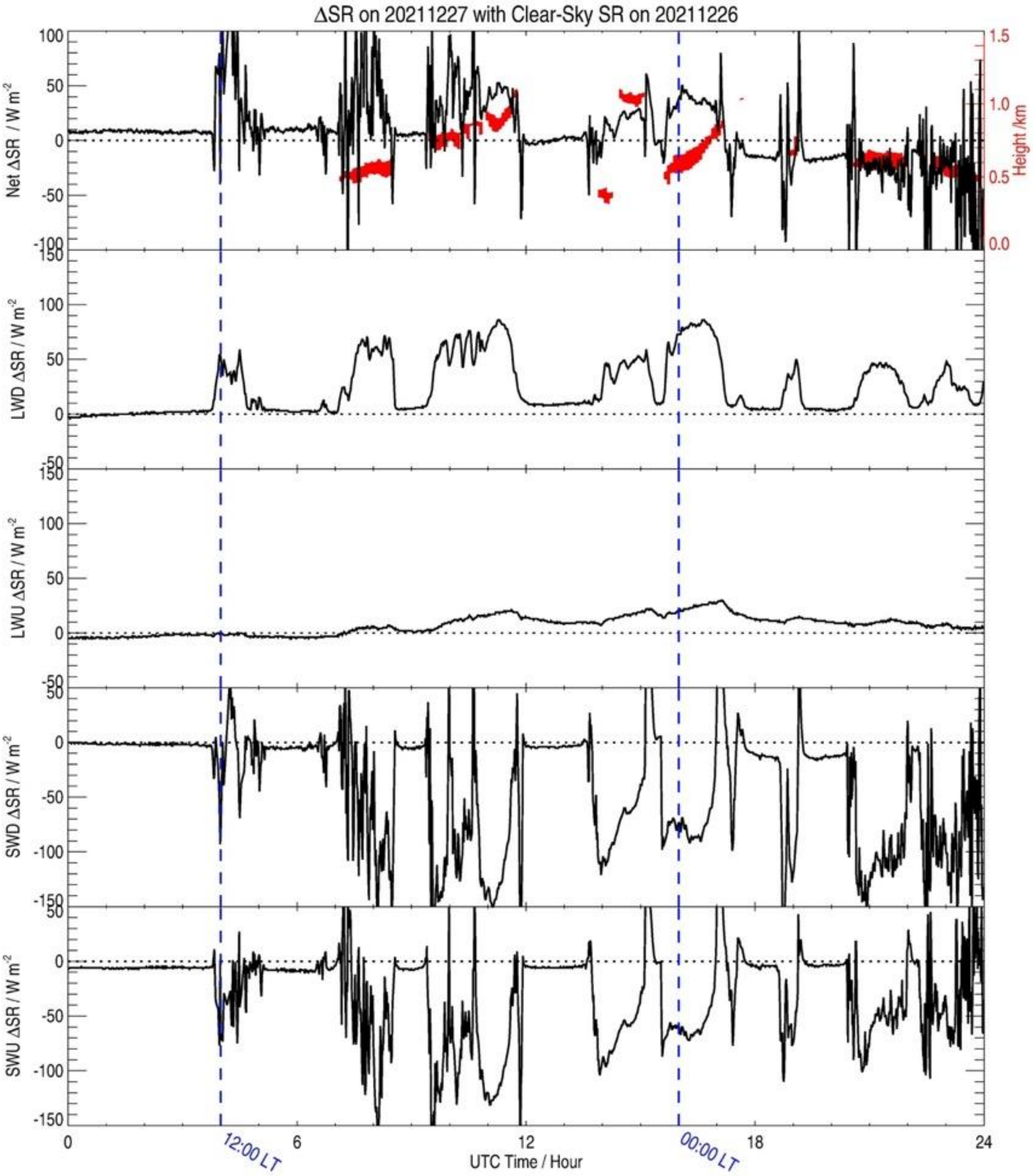

Figure 5: Time evolution (UTC, hour) of the Surface Radiation Anomaly (ΔSR), difference between the SR (W m^{-2}) measured on 27 December 2021 and the reference clear-sky (SR_{Ref}) SR (W m^{-2}) measured on 26 December 2021: (from top to bottom) Net (Net ΔSR), longwave downward (LWD ΔSR), longwave upward (LWU ΔSR), shortwave downward (SWD ΔSR) and shortwave upward (SWU ΔSR). The time evolution of the SLW cloud is highlighted by a red area in the uppermost panel, with the height on the y-axis shown on the right. The 00:00 and 12:00 local times (LT) are highlighted by 2 vertical blue dashed lines.

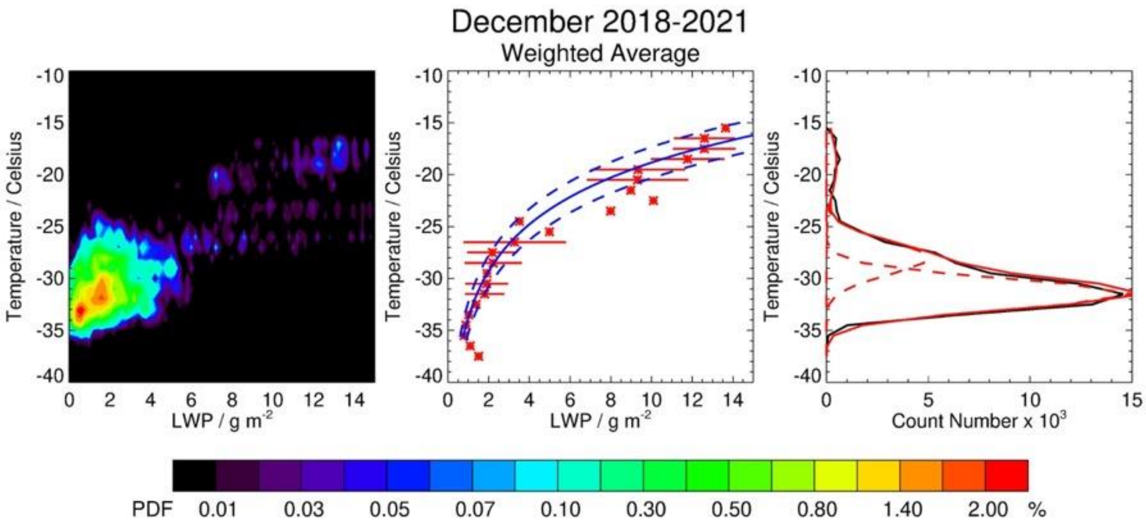

Figure 6: (Left) Probability Density ~~Function~~ (~~PDF,~~ %) of the Temperature (°C) as a function of Liquid Water Path (LWP, g m^{-2}) contained in the Supercooled Liquid Water clouds (SLWCs) above Dome C in December 2018-2021. The ~~PDF~~ Probability Density is defined in the text. (Centre) Weighted-average LWP vs. temperature (red asterisks) with a fitted logarithmic function (blue solid) encompassing the significant points (2 dashed blue lines). Horizontal bars represent 1-sigma variability in LWP per 1°C-wide bin over significant points. (Right) Temperature as a function of count number per 1°C-wide bin (black solid line) with 3 fitted Gaussian functions (red dashed curves). The sum of the 3 Gaussian functions is represented by a red solid line.

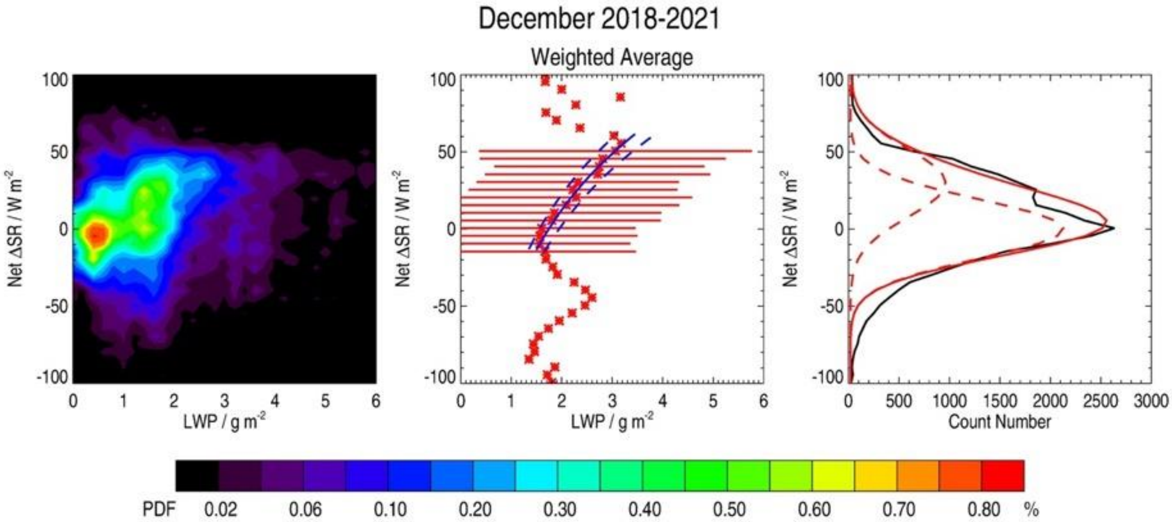

Figure 7: (Left) Probability Density ~~Function~~ (~~PDF,~~ %) of the Net Surface Radiation Anomaly (Net ΔSR, W m^{-2}) as a function of Liquid Water Path (LWP, g m^{-2}) contained in the Supercooled Liquid Water clouds (SLWCs) above Dome C in December 2018-2021. The Probability Density~~PDF~~ is defined in the text. (Centre) Weighted-average LWP vs. Net ΔSR (red asterisks) with a fitted logarithmic function (blue solid) encompassing the significant points (2 dashed blue lines). Horizontal bars represent 1-sigma variability in LWP per 5 W m^{-2}-wide bin over significant points. (Right) Net ΔSR as a function of count number per 5 W m^{-2}-wide bin (black solid line) with 2 fitted Gaussian functions (red dashed curves). The sum of the 2 Gaussian functions is represented by a red solid line.

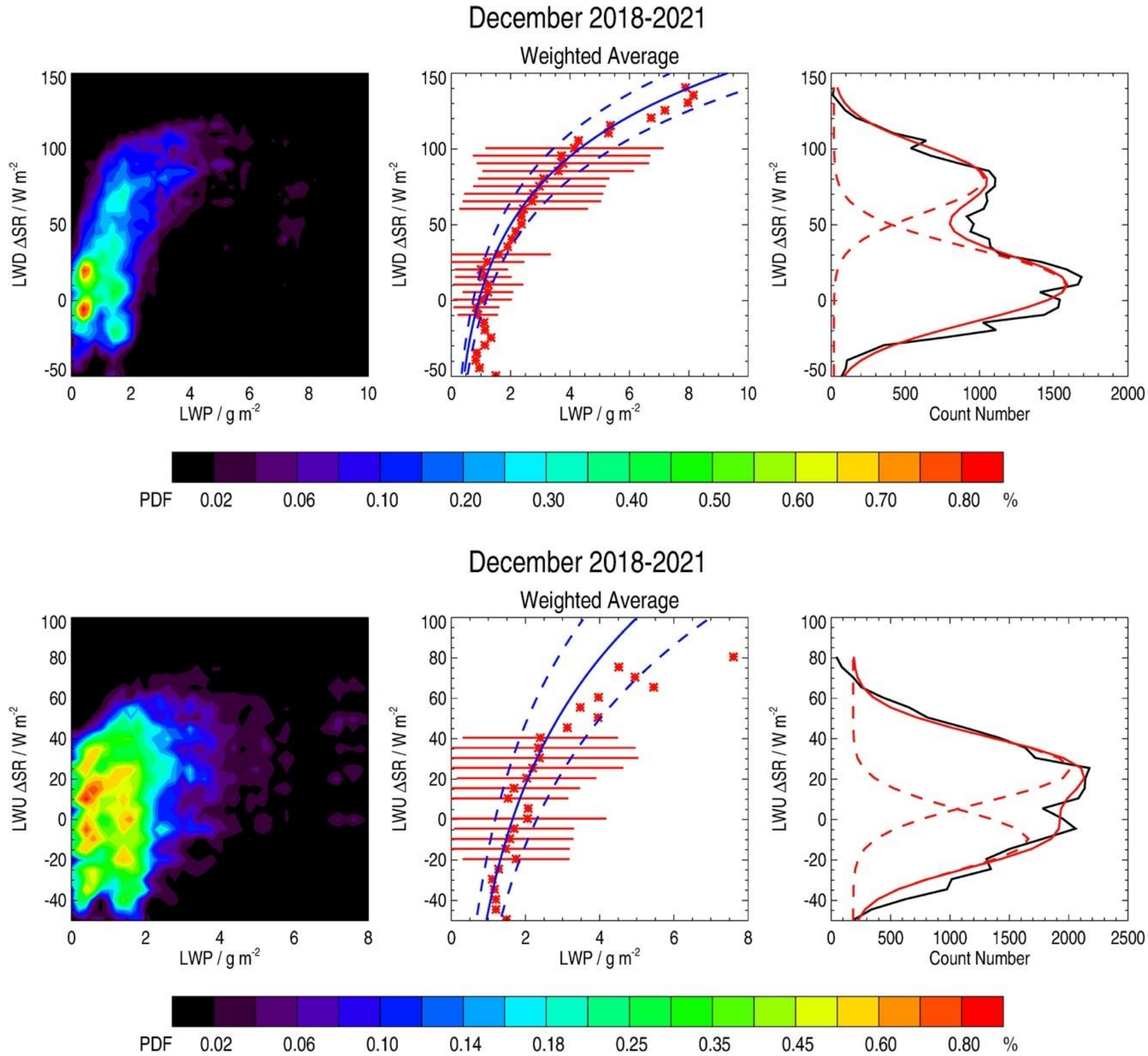

Figure 8: As in Figure 7 but for the Longwave Downward (top) and Upward (bottom) Surface Radiation Anomaly (LWD and LWU ΔSR, respectively).

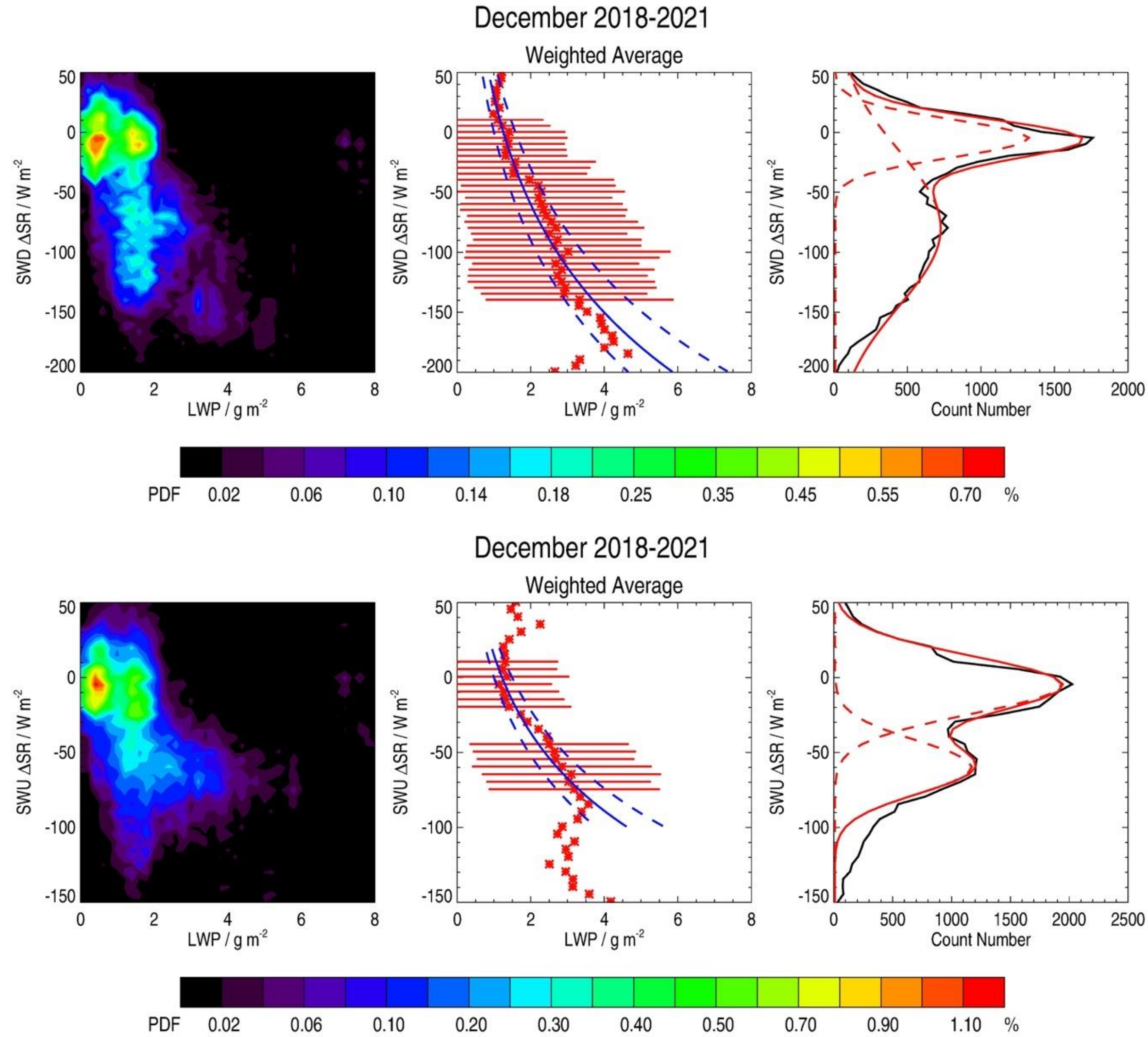

Figure 9: As in Figure 7 but for the Shortwave Downward (top) and Upward (bottom) Surface Radiation Anomaly (SWD and SWU ΔSR, respectively).

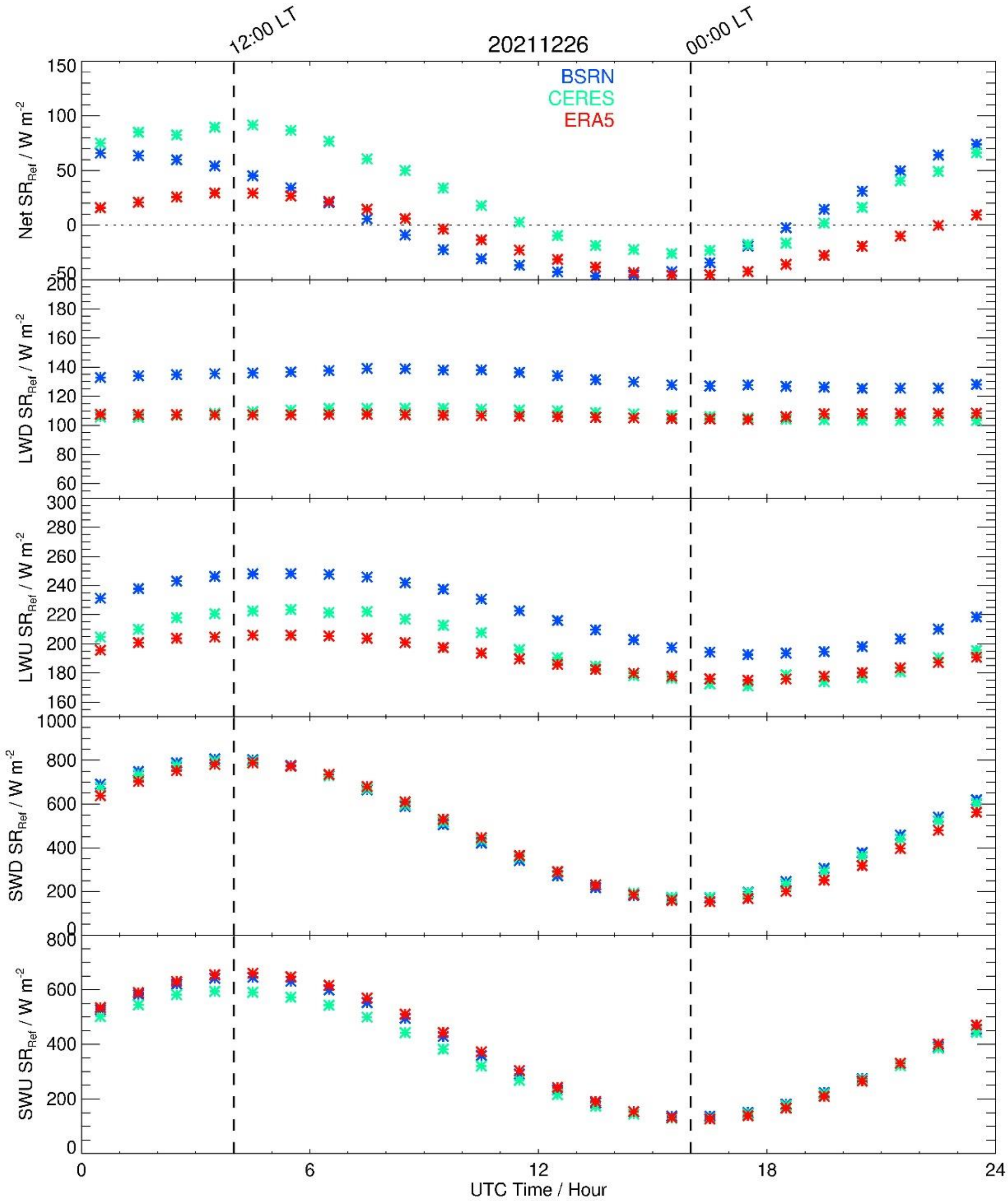

Figure 10: Hourly time evolution (UTC, hour) of the clear-sky surface radiations (SR, W m^{-2}) observed by the BSRN instruments (blue asterisks), the CERES (green asterisks) and the ERA5 (red asterisks) data sets on 26 December 2021: (from top to bottom) Net SR, Longwave Downward SR (LWD SR), Longwave Upward SR (LWU SR), Shortwave Downward SR (SWD SR) and Shortwave Upward SR (SWU SR). The 00:00 and 12:00 local times (LT) are highlighted by 2 vertical dashed lines.

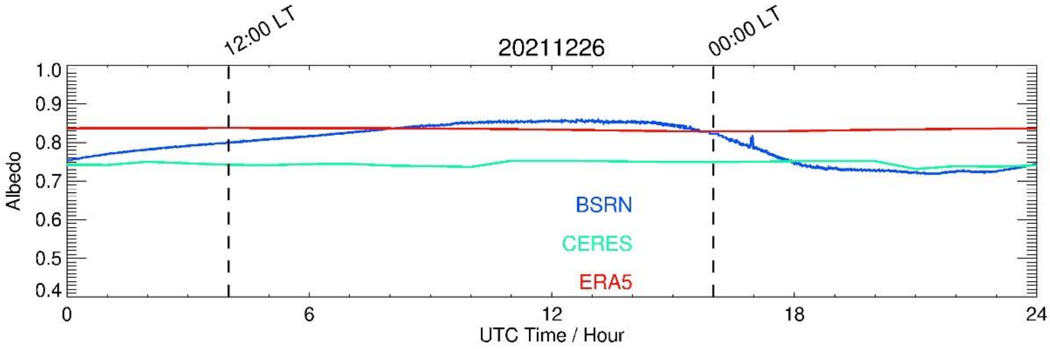

Figure 11: Time evolution (UTC, hour) of the surface albedo observed by the BSRN instruments (blue), the CERES (green) and the ERA5 (red) data sets on 26 December 2021. The 00:00 and 12:00 local times (LT) are highlighted by 2 vertical dashed lines.

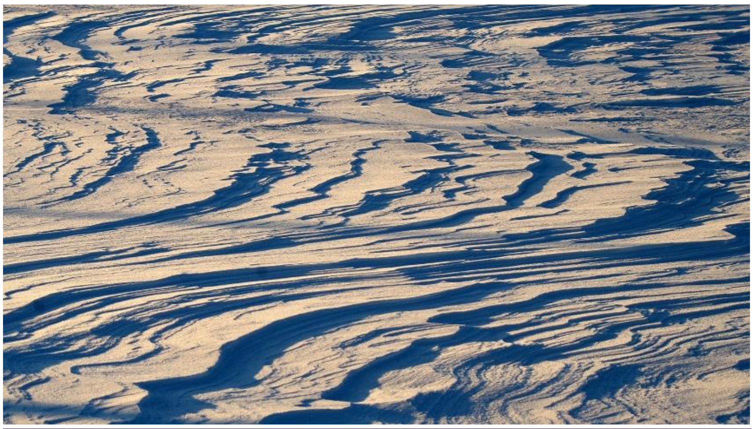

Figure 12: Image of the sastrugi on the ice surface (Wikimedia Commons).

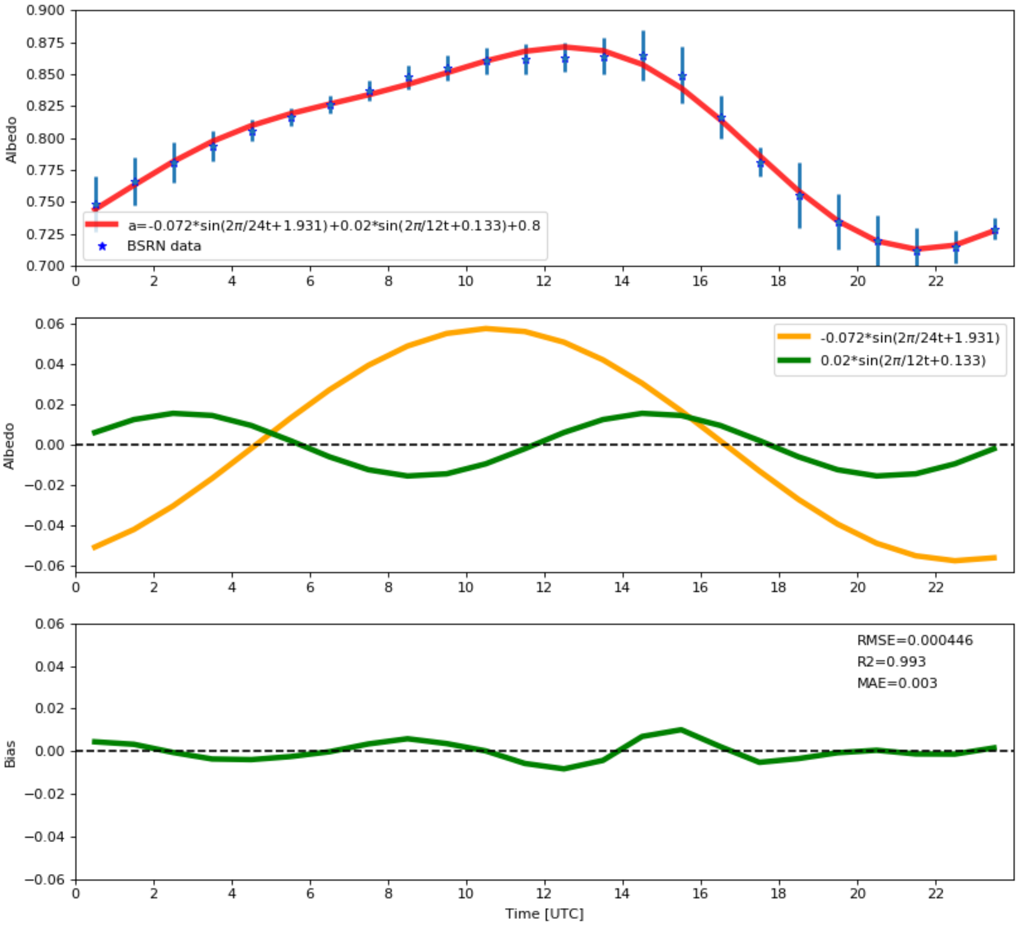

Figure 13: (Top) Hourly time evolution (UTC, hour) of the mean surface albedo observed by the BSRN instruments (blue star) associated with the 5 clear-sky periods under consideration

in our analysis together with the associated standard deviation (vertical bar) together with the fitted trigonometric function based on 2 sine functions (red). (Center) The 2 sine functions fitting the hourly time evolution of the BSRN mean surface albedo. (Bottom) Hourly time evolution (UTC, hour) of the albedo residuals (BSRN-fit) and associated Root Mean Square Error (RMSE), Coefficient of determination (R^2), and Mean Absolute Error (MAE).

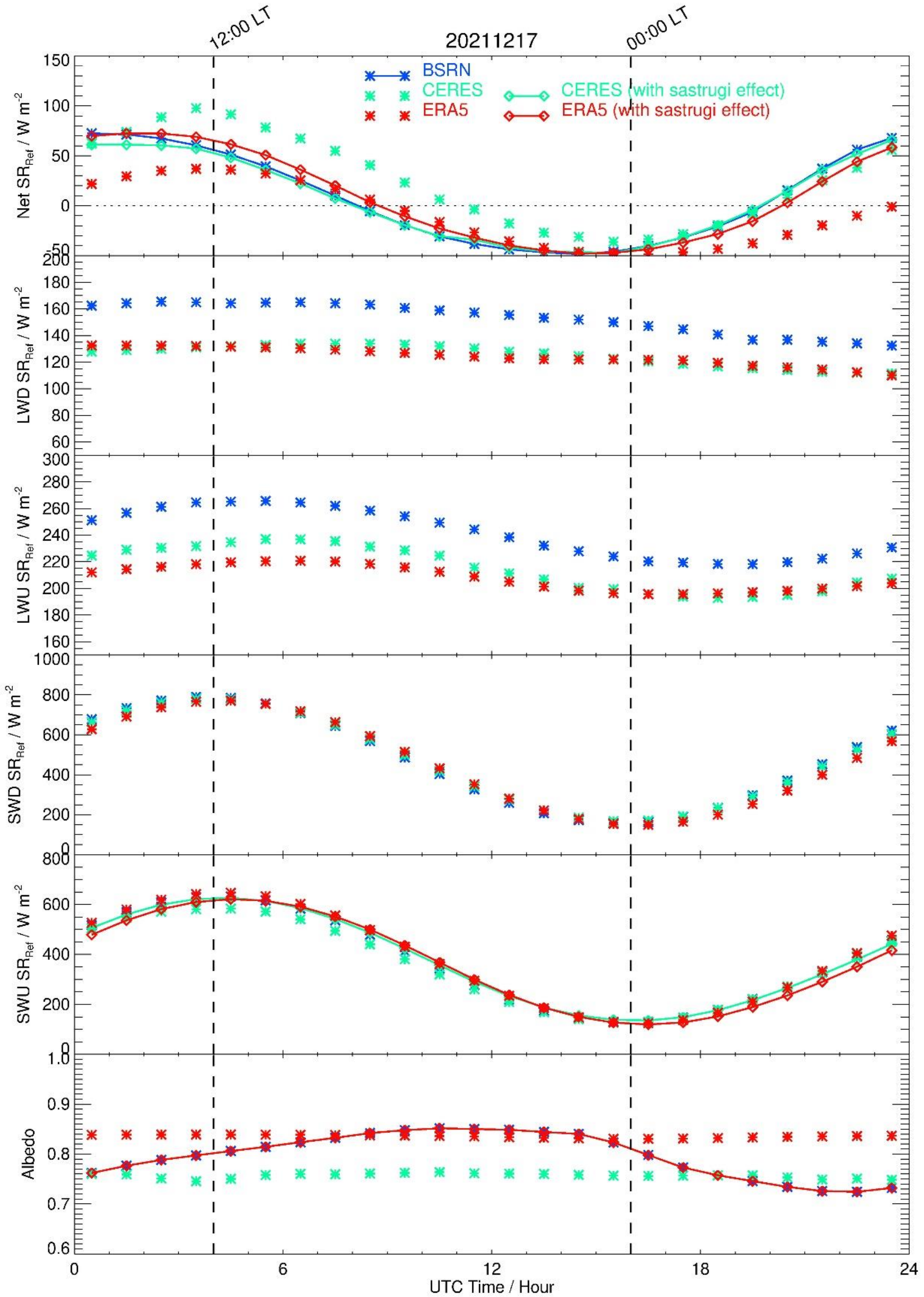

Figure 14: Same as Figure 11 with the albedo inserted in the lowermost panel. Net SR, SWU SR, and albedo including the sastrugi effect for ERA5 (red solid line) and CERES (green solid line) have also been added in the Figures.

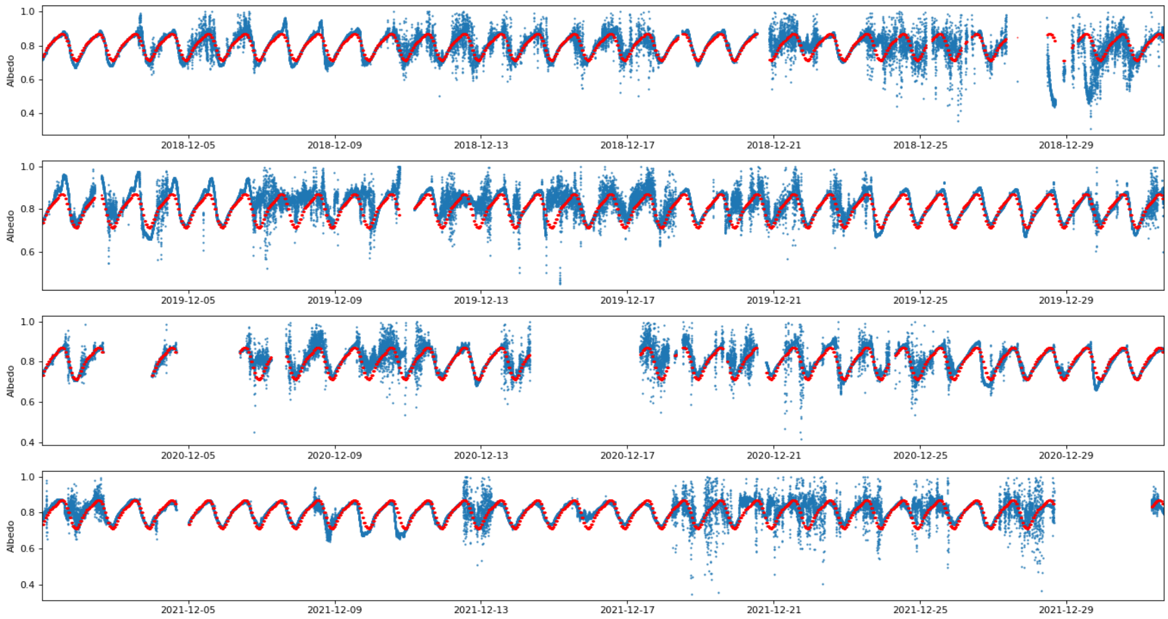

Figure 156: Hourly time evolution (UTC, hour) of the surface albedo observed by the BSRN instruments (blue), and using the fit function based on 2 sine functions (red) for the whole BSRN data set covering the month of December inrs 2018, 2019, 2020 and 2021.